Large Deformation Diffeomorphic Metric Curve Mapping

Joan Glaunès[*†], Anqi Qiu[* ‡§], Michael I. Miller[¶], Laurent Younes[‖]

March 19, 2008

[*]Both authors contributed equally to this work.

[†]MAP5, CNRS UMR 8145, Université Paris Descartes, 75006 Paris, France.

[‡]Correspondence to: Anqi Qiu, Division of Bioengineering, National University of Singapore, 7 Engineering Drive 1, Block E3A 04-15, Singapore 117574. Email: bieqa@nus.edu.sg. Tel: +65 6516 7002. Fax: +65 6872 3069

[§]Division of Bioengineering, National University of Singapore, Singapore, 117574

[¶]Center for Imaging Science, Johns Hopkins University, Baltimore, MD 21218

[‖]Department of Applied Mathematics and Statistics, Johns Hopkins University, Baltimore, MD 21218

Abstract

We present a matching criterion for curves and integrate it into the large deformation diffeomorphic metric mapping (LDDMM) scheme for computing an optimal transformation between two curves embedded in Euclidean space $\mathbb{R}^d$. Curves are first represented as vector-valued measures, which incorporate both location and the first order geometric structure of the curves. Then, a Hilbert space structure is imposed on the measures to build the norm for quantifying the closeness between two curves. We describe a discretized version of this, in which discrete sequences of points along the curve are represented by vector-valued functionals. This gives a convenient and practical way to define a matching functional for curves. We derive and implement the curve matching in the large deformation framework and demonstrate mapping results of curves in $\mathbb{R}^2$ and $\mathbb{R}^3$. Behaviors of the curve mapping are discussed using 2D curves. The applications to shape classification is shown and experiments with 3D curves extracted from brain cortical surfaces are presented.

1 Introduction

Matching curves embedded in $\mathbb{R}^2$ and $\mathbb{R}^3$ is important in the fields of medical imaging and computer vision [1–3]. In medical imaging, the most striking gross morphological features of the cerebral cortex are the sulcal fissures on the cortical surface [4]. They are selected as the basis for structural analysis on the internal surface anatomy of the brain because they separate functionally distinct regions and provide a natural topographic partition of the anatomy. Even though major sulci consistently appear in all anatomies, they exhibit variability in size and configurations [4]. A quantitative study of sulcal anatomical structures

requires developing mathematical models for characterizing shape and geometry of curves, and for accommodating the variability present across populations [5–8]. Moreover, image boundary, contours, and skeletons are often used to represent shapes of objects in many applications of computer vision, such as tracking human body motion in motion tracking, finding correspondence between maps and terrain images, object recognition and classification. All of these formulate two problems: representation of curves and mathematical models of transformations.

In non-rigid registration problems, desired transformations are often constrained to be diffeomorphic — one to one (invertible) and smooth with smooth inverse so that connected sets remain connected, disjoint sets remain disjoint, smoothness of features such as curves is preserved, and coordinates are transformed consistently. Consequently, many researchers have paid great attention to such diffeomorphic transformations particularly in the field of Computational Anatomy for studying the geometric variation of human anatomy (e.g. [9–17]).

Over the past several years we have been using large deformation diffeomorphic metric mapping (LDDMM) [13, 18, 19] to map 3D volume coordinates in the brain as well as in the heart [20]. This method not only provides a diffeomorphic correspondence ϕ between shapes C and S, but defines a metric distance in a shape space as well. The basic diffeomorphic metric mapping approach taken for understanding structures of object shapes is to place the set of objects into a metric space. The idea is to model the mapping of one from the other via a dynamic flow of diffeomorphisms (time dependent deformation) $t \in [0, 1]$ of the ambient space $\mathbb{R}^d$. Instead of working directly in the space of diffeomorphisms, we work with time dependent vector fields, $v_t : \mathbb{R}^d \to \mathbb{R}^d$ for $t \in [0, 1]$, which model the infinitesimal efforts

of the flow. The flow ϕ_t^v is then defined via the differential equation

$$\frac{\partial \phi_t^v}{\partial t} = v_t(\phi_t^v), \tag{1}$$

with $\phi_0^v(x) = x$, and the resulting diffeomorphism is given by the flow at time $t = 1$, ϕ_1^v. In order to ensure that the resulting solution to this equation is a diffeomorphism, v_t must belong to a space, V, of regular vector fields (see [21, 22] for specific requirements), for $t \in [0, 1]$ with $\int_0^1 \|v_t\|_V \, dt < \infty$. V is a Hilbert space with an associated kernel function k_V, and norm $\|\cdot\|_V$. This norm models the infinitesimal cost of the flow.

Assume that for any pair objects of C and S, there exists some vector fields v_t such that the diffeomorphism ϕ_1^v transforms shape C to shape S, which we write $\phi_1^v \cdot C = S$. Then one can look at the optimal vector fields $\hat{v}_t$ satisfying $\phi_1^{\hat{v}} \cdot C = S$ and minimizing the integral of the infinitesimal costs. The metric distance between shapes, $\rho(C, S)$, is defined as the length of the geodesic path $\phi_t^{\hat{v}} \cdot C$ for $t \in [0, 1]$ generated from C to S in the shape space. Such a metric between C and S has the form

$$\rho(C, S) = \inf_{v_t} \left(\int_0^1 \|v_t\|_V^2 \, dt \right)^{\frac{1}{2}} \quad \text{such that } \phi_1^v \cdot C = S \; . \tag{2}$$

In practice, we often define an inexact matching problem: find a diffeomorphism $\hat{\phi}_t$ between two objects C and S as a minimizer of

$$J_{C,S}(\phi_t) \doteq \gamma \rho(C, \phi_1 \cdot C)^2 + E(\phi_1 \cdot C, S).$$

Equivalently, we have $\hat{\phi}_t = \phi_t^{\hat{v}}$, where the vector fields $\hat{v}_t$ minimize the energy

$$J_{C,S}\left((v_t)_{t\in[0,1]}\right) \doteq \gamma \int_0^1 \|v_t\|_V^2 \, dt + E(\phi_1^v \cdot C, S), \tag{3}$$

and γ is a trade-off parameter. The first term in (3) is a regularization term to guarantee the smoothness of deformation fields and the second term is a matching functional to quantify the mismatching between the objects $\phi_1^v \cdot C$ and S.

In this LDDMM framework, two matching techniques are commonly used that result in different models for $E(\phi_1^v \cdot C, S)$. The first one is volume image matching, which works directly with the raw 3D volume images, multi-valued vectors, as well as tensor matrices arising from DTI studies [13, 23–25], but is computationally intensive. The second one is landmark matching which requires a manual or semi-automated selection of landmarks on the images [18]. In the case of brain images, however, landmarks are usually not just isolated points, but lie along sulcal or gyral curves extracted from cortical surfaces which are themselves segmented from the 3D images. In such a situation, the landmark matching tool is commonly used [26, 27]. It is imperfect, however, because it first requires to select the same number of points on both source and target curves, and second it specifies arbitrary correspondences between specific points on these curves, giving artificial constraints to the registration process. To overcome this issue, some new methods were proposed, e.g. using level-sets representations of the curves [28]. In [29], an extension of the LDDMM approach in which shapes are considered as unlabelled sets of landmarks has been proposed. However, as geometric objects, curves or surfaces should not be treated as a sequences of points because the higher order information (tangent vectors or curvature) is discarded when reducing 1D

or 2D manifolds into 0-dimensional point sets. In the case of surfaces, a representation via currents, or vector-valued measures, has recently been developed [30]. It allows to put into the metric both location and tangential information of the surfaces. Tools presented in [29] and [30] actually derive from the same general framework that defines computable metrics on any m-dimensional submanifolds of $\mathbb{R}^d$ with $m \leq d$. The case of curves ($m = 1$) has been introduced shortly in [31, 32]. It is the purpose of this paper to present a full mathematical explanation and derivation of this representation of curves in the LDDMM framework.

This model for curve matching is a special case of a general framework for submanifolds, which could be called measure or current matching, and uses ideas from geometric measure theory and reproducing kernels while setting up into Grenander's theory of deformable templates [9]. Other examples had already been presented: surfaces in [30] and unlabelled point sets (which correspond to the 0-dimensional case) in [29]. In particular, the study and use of the metric distance defined in the shape space for shape analysis has received great attention in computer vision and medical imaging as partly shown here in Section 5. The common approach consists in defining a Riemannian metric on the tangent space to a curve, i.e. the space of infinitesimal transformations of a curve, and extending it to the whole space. Sharon and Mumford [33] proposed a very elegant mathematical model for closed planar curves, which can not be generalized. Younes [34] proposed to use an elastic metric that measures the cost of deformation of the ambient space, which corresponds to the LDDMM setting described previously and considered in the present paper. Recent works [35–37] have emphasized the efficiency of the shape space model or developed its mathematical theory [38]. However these constructions require that a smooth transformation actually exists between any two curves in the space, which usually restricts the study to the subclass of closed, non

crossing curves. Our approach is different in the sense that we do not claim to find exact correspondences between curves, but rather find a diffeomorphic transformation that match two curves up to an acceptable error. What we propose here is a way to compute this error, i.e. a model for evaluating the differences between shapes that remain after matching. It allows to compare curves that may present noisy parts, or be composed of different numbers of connected components, or to match a closed curve to an open curve, etc. Such situations are common in practical applications, which indicates that the curve mapping presented in this paper will be more suitable to applications in computer vision and medical imaging analysis.

This paper is organized as follows. We start with the geometric representation of curves that incorporates the geometry of the curves due to the sensitivity to both location and their tangent vectors (the first order local geometric structure) in Section 2.1. In Section 2.2, we describe that such a representation of curves as mathematical objects provide elements in a vector space equipped with a computable normed distance. In Section 3, "closeness" between two curves is then quantified by the norm-square distance between their associated representations, which serves as matching criterion for finding an optimal transformation from one curve to the other. In Section 3.2, we integrate this matching functional with a variational optimization problem of the LDDMM and compute its gradient with respect to a linear transformation of the velocity, momentum. Appendix B, demonstrates the other use of the matching functional in the derivation of the similarity transformation (rotation, translation, and isotropic scaling). In Section 5, we finally demonstrate the application of this method to curves in $\mathbb{R}^2$ and $\mathbb{R}^3$ and compare matched results and deformation fields between this method and the landmark matching method [18] in the LDDMM framework.

2 Curves as Vector-Valued Measures

We define a norm that quantifies the similarity between two curves by first introducing a geometric representation of the curve and then inducing its norm in a Hilbert space via a differential operator.

2.1 Geometric Curve Representation

We follow the approach presented [30] for surfaces. However, we will not use the term "currents" in this paper, nor use any notion of exterior calculus. Let $C \subset \mathbb{R}^d$ be an open or closed curve. We assume that C is both piecewise C^0 and piecewise C^1, which means that it may be composed of several disconnected components, and may present a finite number of angular points. Let $\gamma_C : [0,1] \to \mathbb{R}^d,\ s \mapsto \gamma_C(s) = [x^1(s), \ldots, x^d(s)]$ be a parametrization of this curve. At almost any point on the curve, the tangent vector is given by $\gamma'_C(s) = [\frac{dx^1}{ds}, \ldots, \frac{dx^d}{ds}]$. The existence of these tangent vectors along the curve gives us a natural action of the curve on vector fields $w : \mathbb{R}^d \to \mathbb{R}^d$ by the rule:

$$\langle \mu_C | w \rangle \doteq \int_0^1 \gamma'_C(s) \cdot w(\gamma_C(s)) ds, \tag{4}$$

where $\cdot$ denotes the dot product in $\mathbb{R}^d$. Intuitively, $\langle \mu_C | w \rangle$ is large when the direction of the vector field $w(x)$ is close to the tangent vectors $\gamma'_C(s)$ along the curve. It is close to zero when $w(x)$ is almost perpendicular to the curve, or when $w(x)$ take small values (in norm) along the curve. Figure 1 demonstrates the evaluation of $\langle \mu_C | w \rangle$ in several cases when $w(x)$ is parallel to the tangents of C (first panel), perpendicular to C (middle panel), and the

norm of $w(x)$ is close to zero along the curve (last panel).

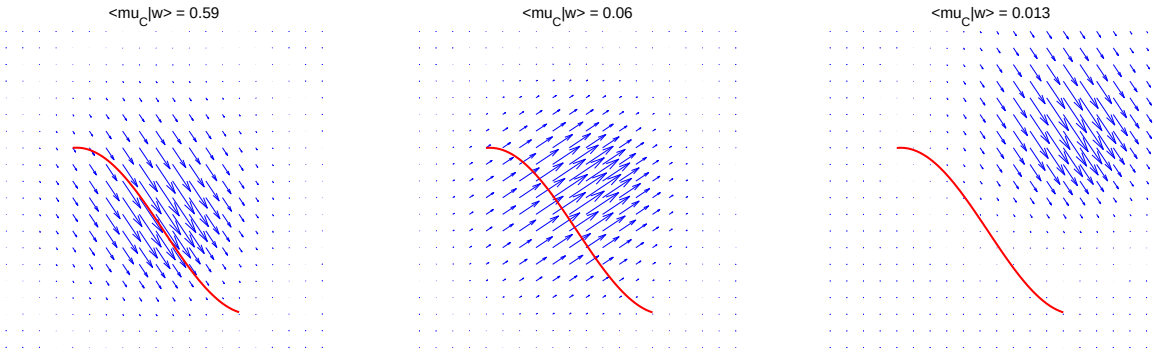

Figure 1: Evaluation of a vector field (blue arrows), $w(x)$, along a curve (in red), C. Left: Directions of vectors match those of the tangents to the curve. Middle: Directions are perpendicular to the curve. Right: Directions match, but norm of vectors are close to zero along the curve.

Hence both location and tangential information of the curve is integrated in this expression. Another important point here is that it is invariant under re-parametrization of the curve, so that if we have a new parameter $t = \psi(s)$, with ψ increasing, it is simple to show that $\langle \mu_C | w \rangle$ is unaffected. However using $t = \psi(s)$ with ψ decreasing will give an opposite value for $\langle \mu_C | w \rangle$, which means that the representation is orientation dependent.

Eq. (4) associates to every oriented curve C a unique representant μ_C which is a linear functional acting on vector fields of $\mathbb{R}^d$. Equivalently, μ_C can be understood as a vector-valued Borel measure. Linear combinations of measures are defined with the rule $\langle \alpha\mu_C + \beta\mu_S | w \rangle = \alpha \langle \mu_C | w \rangle + \beta \langle \mu_S | w \rangle$ for any $\alpha, \beta \in \mathbb{R}$ and curves C, S. In general, these combinations are not associated to any curve, unless $|\alpha| = |\beta| = 1$: for example, $\mu_C - \mu_S$ corresponds to the concatenation of curve C and curve S with opposite orientation.

The advantage here is to embed the curves in a vector space (of vector-valued measures) on which it is possible to use functional analysis tools to define norms and compare curves

via these norms. This will be developed in section 2.2.

2.2 Norm on Vector-Valued Measure

We would like to define a norm that computes a geometrical distance between two curves. For instance, Figure 2 shows two parallel segments C and S with length 1 in $\mathbb{R}^2$, separated

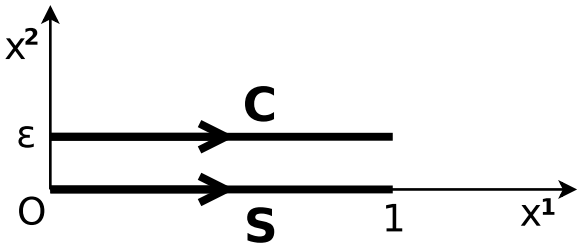

Figure 2: Two parallel segments C and S, separated by a small distance ε.

by a small distance ε. We want the norm of the difference $\mu_C - \mu_S$ of the corresponding vector-valued measures to be small since the segments are close to each other.

This can be achieved if one puts constraints on the variations of the test vector fields w so that the evaluation of the curve representors μ_C and μ_S on w gives close results. To do so, we define a norm on vector fields in the form of

$$\|w\|_W^2 \doteq \int_{\mathbb{R}^d} |Lw(x)|^2 dx \ , \tag{5}$$

where L is a linear differential operator of sufficient order such that the following property on the norm is guaranteed

$$\|w\|_{1,\infty} = \sup_{x\in\mathbb{R}^d} \left\{ |w(x)| + \sum_{i=1}^{d} \left| \frac{\partial w}{\partial x^i}(x) \right| \right\} \leq c_W \|w\|_W \tag{6}$$

for some fixed constant $c_W > 0$. In this setting, test vector fields w will belong to the Hilbert space W associated with the norm $\|\cdot\|_W$.

Proposition 1. *If property in Eq. (6) is satisfied, then the linear functional μ_C defined in Eq. (4) is a continuous linear functional on W.*

Proof. For any $w \in W$,

$$\begin{aligned} |\langle \mu_C | w \rangle| &\leq \int_0^1 |\gamma_C'(s) \cdot w(\gamma_C(s))| ds, \\ &\leq \int_0^1 |\gamma_C'(s)||w(\gamma_C(s))| ds, \\ &\leq \|w\|_{1,\infty} \int_0^1 |\gamma_C'(s)| ds = \|w\|_{1,\infty} l_C, \\ &\leq c_W \|w\|_W l_C, \end{aligned}$$

where l_C is the length of C. □

We can therefor compare vector-valued measures via the dual norm, defined by:

$$\|\mu_C\|_{W^*} \doteq \sup_{\|w\|_W \leq 1} \langle \mu_C | w \rangle .$$

Going back to example of Figure 2, the evaluation of the difference $\mu_C - \mu_S$ is

$$\langle \mu_S - \mu_C | w \rangle = \int_0^1 \gamma_S'(s) \cdot w(\gamma_S(s)) - \gamma_C'(s) \cdot w(\gamma_C(s)) \, ds.$$

With $\gamma_S(s) = (s, 0)$, $\gamma_C(s) = (s, \varepsilon)$, $\gamma_C'(s) = \gamma_S'(s) = (1, 0)$, we get

$$\langle \mu_S - \mu_C | w \rangle = \int_0^1 (w^1(s, 0) - w^1(s, \varepsilon)) \, ds,$$

where $w^1(s,0)$ denotes the first coordinate of vector $w(s,0)$. The integrand $w^1(s,0) - w^1(s,\varepsilon)$ is bounded by $\varepsilon \|w\|_{1,\infty}$, which in turn is bounded by $\varepsilon c_W \|w\|_W$ from property (6). Hence the dual norm $\|\mu_S - \mu_C\|_{W^*}$ is bounded by εc_W. When ε decreases, the norm $\|\mu_C - \mu_S\|_{W^*}$ goes to zero, as expected.

2.3 Explicit expression of the dual norm with kernels

The explicit expression of the dual norm involves the Green's function $k_W(x,y)$ of the operator L^*L, where L^* is the adjoint of L. $k_W(x,y)$ is also the reproducing kernel of the space W. It is defined by the property

$$\int_{\mathbb{R}^d} Lk_W(x,y)\xi \cdot Lw(y)\, dy = \langle k_W(x,\cdot)\xi, w\rangle_W = w(x)\cdot\xi, \tag{7}$$

where $\langle\cdot,\cdot\rangle_W$ represents the inner product of two vector fields in Hilbert space W. Note that since we are dealing with vector fields, $k_W(x,y)$ is a matrix operator, we need to apply it to a vector $\xi \in \mathbb{R}^d$ to get a proper definition.

To fix ideas at this point, one may choose L such that $L^*L = (\mathrm{Id} - \alpha^2\nabla^2)^k$ for some constants $\alpha > 0$ (scale parameter) and integer k, which gives the Sobolev H^k Hilbert space. The corresponding kernel operator has explicit expression in terms of modified Bessel functions of the second kind [39].

Lemma 1. *The norm of the vector-valued measure μ_C in the dual space W^* is equal to*

$$\|\mu_C\|^2_{W^*} = \int_0^1 \int_0^1 \Big[k_W(\gamma_C(s),\gamma_C(r))\ \gamma_C'(s)\Big]\cdot\gamma_C'(r)\ ds\ dr. \tag{8}$$

Proof.

$$\begin{aligned}\langle \mu_C | w \rangle &= \int_0^1 \gamma'(s) \cdot w(\gamma(s)) ds \\ &= \int_0^1 \langle k_W(r(s), \cdot)\gamma'(s), w \rangle_W ds \\ &= \left\langle \int_0^1 k_W(r(s), \cdot)\gamma'(s) ds, w \right\rangle_W\end{aligned}$$

By Cauchy-Schwartz inequality, this achieves the maximum for $\|w\|_W = 1$ if

$$w = \frac{\int_0^1 k_W(\gamma(s), \cdot)\gamma'(s) ds}{\| \int_0^1 k_W(\gamma(s), \cdot)\gamma'(s) ds \|_W}.$$

Therefore, we have

$$\begin{aligned}\|\mu_C\|_{W^*}^2 &= \left\| \int_0^1 k_W(\gamma(s), \cdot)\gamma'(s) ds \right\|_W^2 \\ &= \int_0^1 \int_0^1 \langle k_W(\gamma_C(s), \cdot)\gamma_C'(s), k_W(\gamma_C(r), \cdot)\gamma_C'(r) \rangle_W \; ds \; dr \\ &\overset{(a)}{=} \int_0^1 \int_0^1 \left[k_W(\gamma_C(s), \gamma_C(r)) \; \gamma_C'(s) \right] \cdot \gamma_C'(r) \; ds \; dr \; ,\end{aligned}$$

where (a) follows from the reproducing property of the kernel k_W stated in (7). □

The expression of the dual norm indicates that the central object in computations is the kernel k_W. Mathematically it is possible to build the Hilbert space W and its dual starting from a given positive kernel (without any knowledge of operator L), with enough regularity to satisfy the property in (6). Links between properties of the kernel and properties of the space in this setting can be found in [40]. In short, k_W should be twice differentiable and vanish at infinity up to order 1. If one additionally requires invariance with respect to

rigid motions, one can prove that k_W is defined by two scalar functions $h, h^\perp : \mathbb{R}^+ \to \mathbb{R}$ such that for every $x, y \in \mathbb{R}^d$, $k_W(x,y)\alpha = h(|x-y|^2)\alpha$ if α is colinear to $x-y$, and $k_W(x,y)\alpha = h^\perp(|x-y|^2)\alpha$ if $\alpha \cdot (x-y) = 0$. For our applications we only consider "scalar" kernels $k_W(x,y) = h(|x-y|^2)\mathrm{I}_d$ i.e. such that $h = h^\perp$, and in practice we tried Gaussian $h(r^2) = e^{-r^2/\sigma_W^2}$ and Cauchy $h(r^2) = \frac{1}{1+r^2/\sigma_W^2}$ kernels. However it would be interesting to study the effect of using non scalar kernels.

3 Curve matching via deformation maps

3.1 A general variational formulation

In the previous section, we introduced representations of curves by vector-valued measures and defined a computable norm in the space of measures to compare them. These tools give us a practical way to define a matching functional between two curves C and S in $\mathbb{R}^d$. Let $\phi : \mathbb{R}^d \to \mathbb{R}^d$ be a deformation map which is supposed to give an approximate correspondence between C and S. The accuracy of this matching can be measured by:

$$E(\phi(C), S) \doteq \left\| \mu_{\phi(C)} - \mu_S \right\|_{W^*}^2 \tag{9}$$

which can be rewritten in terms of kernel k_W, according to Eq. (8),

$$\begin{aligned} E(\phi(C), S) \;=\; & \int_0^1 \int_0^1 \Big[k_W(\gamma_{\phi(C)}(s), \gamma_{\phi(C)}(r))\, \gamma'_{\phi(C)}(s) \Big] \cdot \gamma'_{\phi(C)}(r)\, ds\, dr \\ & -2 \int_0^1 \int_0^1 \Big[k_W(\gamma_{\phi(C)}(s), \gamma_S(r))\, \gamma'_{\phi(C)}(s) \Big] \cdot \gamma'_S(r)\, ds\, dr \\ & + \int_0^1 \int_0^1 \Big[k_W(\gamma_S(s), \gamma_S(r))\, \gamma'_S(s) \Big] \cdot \gamma'_S(r)\, ds\, dr. \end{aligned}$$

The first and last terms are intrinsic energies of the two curves. Roughly, the more curved they are, the higher energy they possess, since flat shaped parts of the curves tend to vanish in the space of vector-valued measures. The middle term penalizes to mismatching between tangent vectors of S and those of $\phi(C)$.

Optimal matching between curves will be defined via minimization of a functional composed of the matching term E and optionally a regularization term to guarantee smoothness of the transformations. We model deformation maps ϕ in the LDDMM framework. Certainly any other model of transformations could be directly applied at this point. For instance, the similarity transformation (rotation, translation, and uniform scale) is derived in Appendix B.

3.2 Large Deformation Diffeomorphic Metric Curve Mapping

In the LDDMM setting, we define the optimal matching, $\hat{\phi}$ between two curves C and S as $\hat{\phi} = \phi_1^{\hat{v}_t}$, $\hat{v}_t$ being the minimizer of the energy

$$J_{C,S}\left((v_t)_{t\in[0,1]}\right) \doteq \gamma \int_0^1 \|v_t\|_V^2 \, dt + \left\|\mu_{\phi_1^v(C)} - \mu_S\right\|_{W^*}^2 \tag{10}$$

and ϕ_1^v is defined in (1).

The first term is the regularization term which controls the smoothness of the diffeomorphism, and the second term is the data attachment to quantify mismatching between deformed C and S. A general result [21, 22] guarantees existence of the solution to this minimization problem.

In [31], such variational problems for 2D curve matching in the large deformation frame-

work were studied, and precise forms of the optimal solutions were given. In this paper we will focus on the discrete formulation, leading to a practical matching algorithm.

4 The discrete model

4.1 Representation with vector-valued Dirac functionals

First suppose that the curve C is continuous and discretized in a sequence of points $\mathbf{x} = (x_1, \ldots, x_n)$ such that each x_i belongs to the curve: for any parametrization γ_C we have $x_i = x_{s_i}$ for $s_i \in [0, 1]$. We do not make any assumption on the way points x_i are distributed along the curve. If C is a closed curve then we assume $x_n = x_1$. We can associate to this sequence of points a specific measure given by vector-valued Diracs:

$$\mu_{\mathbf{x}} = \sum_{i=1}^{n-1} \tau_{\mathbf{x},i} \delta_{c_{\mathbf{x},i}},$$

where $c_{\mathbf{x},i} = \frac{1}{2}(x_i + x_{i+1})$ is the center between points of x_i and x_{i+1}, and $\tau_{\mathbf{x},i} = x_{i+1} - x_i$ gives an approximate tangent vector. This vector-valued measure is also defined by its pairing with smooth vector fields w:

$$\langle \mu_{\mathbf{x}} | w \rangle = \sum_{i=1}^{n-1} \tau_{\mathbf{x},i} \cdot w(c_{\mathbf{x},i}).$$

The important point here is that both the curves and their discrete representants (possibly with different sampling rates) are embedded into the same space of vector-valued measures. Hence it will be possible to compare them via the dual norm introduced earlier.

If C is piecewise continuous, we build a discrete representation by summing the discrete

measures $\mu_{\mathbf{x}}$ corresponding to each connected component.

4.2 Expression of the dual norm

The dual norm of the discrete representant $\mu_{\mathbf{x}}$ expresses conveniently in terms of the kernel k_W:

$$\|\mu_{\mathbf{x}}\|_{W^*}^2 = \left\| \sum_{i=1}^{n} \tau_{\mathbf{x},i} \delta_{c_{\mathbf{x},i}} \right\|_{W^*}^2 = \sum_{i=1}^{n} \sum_{j=1}^{n} \left[k_W(c_{\mathbf{x},i}, c_{\mathbf{x},j})\ \tau_{\mathbf{x},i} \right] \cdot \tau_{\mathbf{x},j}. \tag{11}$$

Note that this is not an approximation of the dual norm, but an exact expression of the dual norm of the discrete approximation of the curve. The following theorem shows that this discrete representant is a good approximation of the curve in space W.

Theorem 1. *If the length of the piece of curve connecting two consecutive points $d_C(x_i, x_{i+1}) = \int_{s_i}^{s_{i+1}} |\gamma_C'(s)| ds$ is bounded by δ, then $\|\mu_x - \mu_C\|_{W^*} \leq c_W \delta l_C$.*

Proof. For any $w \in W$,

$$\begin{aligned}
\langle \mu_{\mathbf{x}} - \mu_C | w \rangle &= \langle \mu_{\mathbf{x}} | w \rangle - \langle \mu_C | w \rangle \\
&= \sum_{i=1}^{n} \tau_i \cdot w(c_i) - \int_0^1 \gamma_C'(s) \cdot w(\gamma_C'(s)) ds \\
&= \sum_{i=1}^{n} \left(\tau_i \cdot w(c_i) - \int_{s_i}^{s_{i+1}} \gamma_C'(s) \cdot w(\gamma_C'(s)) ds \right).
\end{aligned}$$

We have $\tau_i = \gamma_C(s_{i+1}) - \gamma_C(s_i) = \int_{s_i}^{s_{i+1}} \gamma_C'(s)ds$, so we can write:

$$\begin{aligned}\langle \mu_{\mathbf{x}} - \mu_C | w \rangle &= \sum_{i=1}^{n} \int_{s_i}^{s_{i+1}} \gamma_C'(s) \cdot (w(c_i) - w(\gamma_C'(s)))\, ds \\ &\leq \sum_{i=1}^{n} \int_{s_i}^{s_{i+1}} |\gamma_C'(s)||w(c_i) - w(\gamma_C'(s))| ds.\end{aligned}$$

Now $|w(c_i) - w(\gamma_C'(s))| \leq |||w||_{1,\infty}|c_i - \gamma_C'(s)| \leq c_W\|w\|_W\delta$, so we get

$$\begin{aligned}\langle \mu_{\mathbf{x}} - \mu_C | w \rangle &\leq c_W\|w\|_W\delta \sum_{i=1}^{n} \int_{s_i}^{s_{i+1}} |\gamma_C'(s)| ds \\ &\leq c_W\|w\|_W\delta l_C.\end{aligned}$$

□

4.3 Matching functional, discrete case

When curves C and S are discretized by point sequences $\mathbf{x} = (x_i)_{i=1}^n$ and $\mathbf{y} = (y_j)_{j=1}^m$, the sequence of transformed points $\mathbf{z} = (\phi(x_i))_{i=1}^n$ gives a discretization of the deformed curve $\phi(C)$. Here we will derive algorithms based on the following matching functional:

$$E(\mathbf{z}, \mathbf{y}) \doteq \left\| \sum_{i=1}^{n} \tau_{\mathbf{z},i}\delta_{c_{\mathbf{z},i}} - \sum_{j=1}^{m} \tau_{\mathbf{y},j}\delta_{c_{\mathbf{y},j}} \right\|_{W^*}^2, \tag{12}$$

which is explicitly

$$
\begin{aligned}
E(\mathbf{z},\mathbf{y}) \;=\; & \sum_{i=1}^{n-1}\sum_{j=1}^{n-1}\Big[k_W(c_{\mathbf{z},i},c_{\mathbf{z},j})\tau_{\mathbf{z},i}\Big]\cdot\tau_{\mathbf{z},j} - 2\sum_{i=1}^{n-1}\sum_{j=1}^{m-1}\Big[k_W(c_{\mathbf{z},i},c_{\mathbf{y},j})\tau_{\mathbf{z},i}\Big]\cdot\tau_{\mathbf{y},j} \\
& + \sum_{i=1}^{m-1}\sum_{j=1}^{m-1}\Big[k_W(c_{\mathbf{y},i},c_{\mathbf{y},j})\tau_{\mathbf{y},i}\Big]\cdot\tau_{\mathbf{y},j}\ .
\end{aligned}
$$

Note that curves C and S are not necessarily discretized into the same number of points from the above equation. This expression was also given in [32]. We show the derivation of gradient of $E(\mathbf{z},\mathbf{y})$ with respect to ϕ in Appendix A.

4.4 LDDMM Variational Formulation in the discrete setting

Let $\mathbf{x} = (x_i)_{i=1}^n$ and $\mathbf{y} = (y_i)_{i=1}^m$ be discrete samples of curves C and S respectively, and define the trajectories $x_i(t) \doteq \phi_t(x_i)$ for $i = 1,\dots,n$. The optimal matching between samples $\mathbf{x}$ and $\mathbf{y}$ will be defined as a minimizer of

$$
J = \gamma\int_0^1 \|v_t\|_V^2\,dt + \left\|\sum_{i=1}^n \tau_{\mathbf{z},i}\delta_{c_{\mathbf{z},i}} - \sum_{j=1}^m \tau_{\mathbf{y},j}\delta_{c_{\mathbf{y},j}}\right\|_{W^*}^2, \tag{13}
$$

where $\mathbf{z} = (\phi_1(x_i))_{i=1}^n = (x_i(1))_{i=1}^n$. The second term of J depends only on the positions of the finite number of points $(\phi_1(x_i))_{i=1}^n$. In such a situation, like all point-based matching problems in the large deformation setting [18, 19], the following reasoning apply: starting from any arbitrary state $\hat{v}_t$ of the time-dependant vector fields, let us find the optimal vector fields v_t that keep trajectories $x_i(t) = \phi_t^{\hat{v}_t}(x_i)$ unchanged and minimize the functional. Since trajectories are fixed, in particular the end-points $(x_i(1))$ are also fixed; hence the second term of J is constant for this sub-problem and we are left to find vector fields which minimize

the V-norm and satisfy for each time t and each $1 \leq i \leq n$ the constraint $v_t(x_i(t)) = \dot{x}_i(t)$ where $x_i(t)$ are the fixed trajectories. This is a classical interpolation problem in a Hilbert space setting, for which the solution is expressed as a linear combination of spline vector fields involving the kernel operator k_V:

$$v_t(x) = \sum_{i=1}^{n} k_V(x_i(t), x)\alpha_i(t) \ , \tag{14}$$

where $\alpha_k(t)$ are referred to as *momentum vectors*. These vectors can be computed from trajectories $x_i(t)$ by solving the system of linear equations

$$\frac{dx_i(t)}{dt} = \sum_{j=1}^{n} k_V(x_j(t), x_i(t))\alpha_j(t), \qquad i = 1, \ldots, n. \tag{15}$$

Now coming back to the main variational problem, we can restrict the domain of minimization to the subspace of vector fields of the form given by expression in Eq. (14), and choose either trajectories $x_i(t)$ or momentum $\alpha_i(t)$ as minimization variables. The choice of $\alpha_i(t)$ avoids the inversion of linear systems, since in this case Eq. (15) is seen as an ODE system in the unknown $x_i(t)$. The regularization term can be rewritten as a function of variables $\alpha_i(t)$ and $x_i(t)$. From Eq. (14) and the reproducing property of kernel k_V, we get

$$\int_0^1 \|v_t\|_V^2 \, dt = \int_0^1 \sum_{i=1}^{n}\sum_{j=1}^{n} \langle k_V(x_i(t), \cdot)\alpha_i(t), k_V(x_j(t), \cdot)\alpha_j(t)\rangle_V \, dt \tag{16}$$

$$= \int_0^1 \sum_{i=1}^{n}\sum_{j=1}^{n} \Big[k_V(x_j(t), x_i(t))\alpha_j(t)\Big] \cdot \alpha_i(t) dt = \int_0^1 \sum_{i=1}^{n} \alpha_i(t) \cdot \frac{dx_i(t)}{dt} dt \tag{17}$$

Hence the explicit expression of functional in Eq. (13) is the following:

$$
\begin{aligned}
J((\alpha_i(t))) &= \gamma \int_0^1 \sum_{i=1}^{n}\sum_{j=1}^{n} \Big[k_V(x_j(t),x_i(t))\alpha_j(t)\Big]\cdot\alpha_i(t)dt + \\
&\sum_{i=1}^{n-1}\sum_{j=1}^{n-1}\Big[k_W(c_{\mathbf{z},i},c_{\mathbf{z},j})\tau_{\mathbf{z},i}\Big]\cdot\tau_{\mathbf{z},j} - 2\sum_{i=1}^{n-1}\sum_{j=1}^{m-1}\Big[k_W(c_{\mathbf{z},i},c_{\mathbf{y},j})\tau_{\mathbf{z},i}\Big]\cdot\tau_{\mathbf{y},j} \quad (18)\\
&+\sum_{i=1}^{m-1}\sum_{j=1}^{m-1}\Big[k_W(c_{\mathbf{y},i},c_{\mathbf{y},j})\tau_{\mathbf{y},i}\Big]\cdot\tau_{\mathbf{y},j}\ .
\end{aligned}
$$

The derivation of the gradient of J with respect to $\alpha_i(t)$ is given in appendix D.

4.5 Algorithm

We used a conjugate gradient routine to perform the minimization of functional J in (18) with respect to variables $\alpha_i(t)$. Of course any other optimization scheme could be considered at this point. The different steps required to compute the functional and its gradient for each iteration are the following:

1. from momentum vectors $\alpha_i(t)$, compute trajectories $x_i(t)$ by integrating the system of ordinary differential equations (ODE) using Eq. (15).

2. evaluate J from Eq. (18)

3. compute vectors $\eta_i(t)$ by integrating the system of ODE in Eq. (28) in Appendix D.

4. compute gradient $(\nabla J)_i(t) = 2\gamma\alpha_i(t) + \eta_i(t)$.

All time-dependant variables were evaluated on a uniform grid $t_1 = 0, \ldots, t_T = 1$ and a predictor/corrector centered Euler scheme was used to solve the systems of ODE in Eq.

(15) and (28). The complexity of each iteration is of order dTN^2, where $N = \max(n, m)$. To speed up computations when N is large, all convolutions by kernels k_V and k_W are accelerated with a multipole method [41], which reduces the complexity to $dTN\log(N)$.

5 Results

In our experiments, we first used the similarity transformation to transform curves into the same orientation and scale, as described in Appendix B. Then, we applied the curve matching under the LDDMM setting to deform one curve to the other. Kernels of $k_V(x, y)$ and $k_W(x, y)$ were radial with the form $e^{-\frac{|y-x|^2}{\sigma^2}} I_d$, where I_d is the $d \times d$ identity matrix. σ_V and σ_W represent the kernel sizes of k_V and k_W, respectively. They were experimentally adjusted.

5.1 2D Curve Matching

Examples

Shown in Figure 3 are two-dimensional examples where the shape of curves represent bones (the first row), or birds (the second row), or hands (the third row). In this experiment, we chose $\sigma_V = 0.25$ and $\sigma_W = 0.1$ and deformed source shapes to target shapes. The first column shows the target shape, while the rest columns show source shapes. In each panel of the second and third rows, the blue curve represents the source shape before the curve matching and the green curve represents the deformed source shape after the curve matching. The background grid shows the deformation field. Figure 4 shows the time sequence of deformation of the source configuration. The first panel shows the source hand in green and

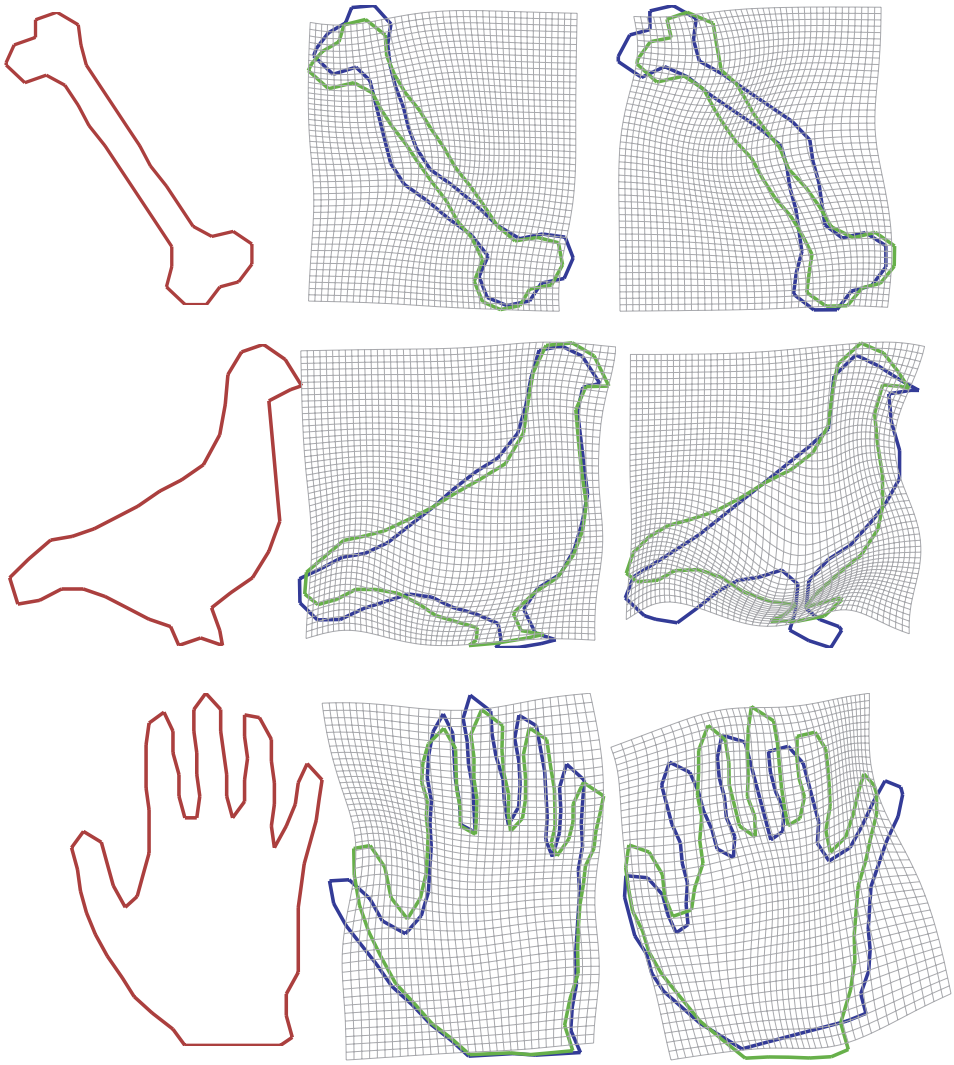

Figure 3: Examples for plane curve matching. Bone, bird, and hand examples are respectively shown in rows. The first column shows target shapes. The second and third columns show source shapes. Blue curves are source shapes, while green curves are deformed source shapes.

the target hand in red. The last panel illustrates how close the deformed source curve (green) are to the target curve (red) after the curve matching. The middle panels demonstrate the smooth deformation as the source hand moves to the target hand along the time.

Robustness Against Noise

One application of studying transformations is to classify objects into different shape

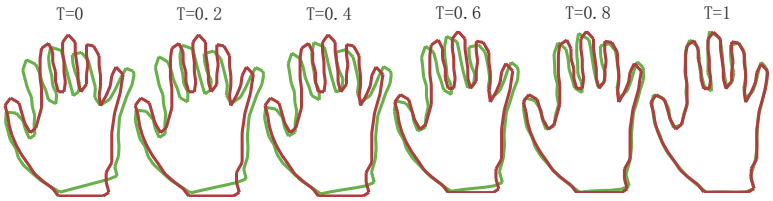

Figure 4: Panels from the left to the right depict the sequence of geodesic mappings connecting the source hand to the target hand at time $t = 0, 0.2, 0.4, 0.6, 0.8, 1$. The source shape and target shape are respectively represented in green and red.

groups. In our LDDMM framework, the velocity vectors transform one object to the other object and give the shortest geodesic path connecting these two objects. The length of the geodesic path defines a metric distance given in (2) and feature in classification. As the purpose of classification, the metric distance should be robust against noise to achieve accurate classification. In this section, we claim that the curve matching provides a more accurate metric distance measurement and overcomes noise effect on matching results compared with the landmark matching [18, 42] when outliers are chosen as landmark points.

Example A in Figure 5 shows boats without and with a mast as the source and target curves in panels (a,b), respectively. The curve and landmark matchings are applied to transforming the source boat to the target boat and results are shown in panels (c,d). The matching term in (18) for the template is near to zero in the region of the mast so that there is no force to drive the source boat to match the mast. The peak point of the mast is chosen as landmark in the landmark matching procedure so the source boat is deformed to the target boat at the mast. However, the metric distance (1.63) in the landmark matching is significantly larger than the one (0.13) in the curve matching. If a threshold is selected to classify these boats, the landmark matching probably considers them in different shape categories while the curve matching recognizes them as boats. When classifying shapes this

problem typically arises as the result of imperfect extraction. The curve matching has less noise effect on the metric distance compared with the landmark matching. A similar example is given in Figure 5 B, one curve without a gap (source shape) and the other with a small gap (target shape). The metric distance (1.37) in the landmark matching is larger than the one (0.72) in the curve matching.

Box bump experiment

To study the behaviour of our curve matching algorithm, we computed matchings between two shapes (cyan and red curves in Figure 6) composed of a box with a semi-circle. Each row in Figure 6 shows one example representing the time evolution of the optimal diffeomorphism by green curve in each panel. The desired behaviour, in which the bump slides along the edge, occurs only when the bumps locations on the two shapes are close (see the top row of Figure 6). Otherwise the deformation that flattens one bump and reforms the other one is prefered, because the deformation cost is lower (see the bottom row of Figure 6. Note again that our algorithm matches shapes up to a small error, measured by the metric W^*. Avoiding such solutions would require to put higher-order (typically curvature) information into the metric W^*, while our metric only relies on tangential information.

Computing all pairwise matchings between 17 shapes composed of a box with a semi-circle when the locations of the bump on each curve subsequently moves further away, we mapped the resulting distance matrix into a 2-dimensional coordinate system using classical multidimensional scaling (MDS) [43]. Figure 7 shows the locations of each shape in the first two scaling dimensions. This confirms the previous analysis: while shapes are correctly ordered into a sequence, they seem to follow a highly curved path, because the "flatten and reform" solutions bound the metric distances between shapes.

Classification

We demonstrate pattern classification of metric distances among curves shown in Figure 8. The shapes in Figure 8 were chosen from hand (10), dude (10), turtle (7), and fish (5) . Special cases (hands and dudes with noise effect) are shown in the last two columns of rows (a,b), which are similar cases as in Figure 5. The reason for choosing fish and turtles is that some of fish are outliers which are similar to turtles.

Our classification approach has three steps: map any two curves to each other and compute metric distances between them using (2), map metric distances into Euclidean space via MDS [43], classify shapes via K-means clustering. Figure 9 shows the scatter plot of the curves in the features spaces generated from MDS. The numbers (1,2,3,4) give the classification results and respectively denote the categories of hand, turtle, fish, and dude. Only two curves were wrongly classified as turtles. One is the hand shown in the second column from the right in row (a), the other is the fish shown in the last column of row (d). As we mentioned in the previous section, the small noise (e.g. the hand and dude in the last column of rows (a,b)) does not inference the classification using the curve matching approach. The successful performance rate of our classification approach is 93.75%.

5.2 3D Curve matching

In this section, we illustrate matching results of 3D curves. All curves were extracted from brain cortical surfaces and matched to the template curve. For the purpose of visualization, we show deformed brain surfaces where the deformation fields obtained from the curve matching were interpolated.

Examples

One major application of the curve matching in medical imaging is to transform one anatomical structure to the other using anatomical curve information. For instance, curves in the brain anatomy can be sulci or gyri that are conventional boundaries of cortical regions. In this experiment, we demonstrate how to warp one cortical surface to the other using the curve matching method. Cortical surfaces shown in the following were generated from MRI image volumes. A 3D subvolume encompassing the region of interest (ROI) was defined manually in each volume. A Bayesian segmentation using the expectation-maximization algorithm to fit the compartmental statistics was used to label voxels in the subvolume as gray matter (GM), white matter (WM), or cerebrospinal fluid (CSF) [44, 45]. Surfaces were then generated at the GM/WM interface using a topology-correction method and a connectivity-consistent isosurface algorithm [46, 47].

Figure 10(a) shows the target of planum temporale (PT) surface located on the superior temporal gyrus (STG) posterior to the Heschl's sulcus (HS) and extending to Sylvian fissure (SF). The structure of PT can be determined by three principal curves (STG, HS, SF) tracked by dynamic programming [48]. In this experiment, we fixed one surface as the target PT surface shown in Figure 10(a). We extracted the three curves from twenty PT surfaces as curve objects and registered them with the curves on the target curves using our curve matching algorithm. Finally, the deformation field was interpolated to the interior region of PTs. The columns from left to right on rows (a)-(d) in Figure 11 respectively illustrate the source PT surface, deformed source PT, source PT superimposed with the target PT, and deformed source PT with the target PT. As shown in Figure 11, the performance for this dataset was quite good. Panel (a) in Figure 13 shows cumulative distance distributions before

and after the matching process. The cumulative distance distribution plots the percentage of vertices whose distance to the target surface is less than d as a function of distance d. Gray curves correspond to the source surfaces, while black curves are for the deformed source surfaces after the matching. Red curves are the mean surface distance graphs before and after the matching process from the bottom to the top, respectively. It is obvious that more vertices move close to the target surface after the matching.

We applied the same strategy to match ten cingulate gyri (CG) to the target CG shown in panel (d) of Figure 12. CG is a part of the limbic cortex and has functions related to symptoms of Schizophrenia and Alzheimer's disease. Panel (b) in Figure 10 shows the six curves defined on the target CG. Each curve is color coded with the index in the same color scheme. Panels (a)-(c) in Figure 12 give examples of the source CG surfaces and their deformed versions. To validate the matched results, we also computed the cumulative distance distributions shown in panel (b) of Figure 13. This set of the CG curve mapping results have been used to detect the group differences in the CG thickness between healthy comparison controls and patients with schizophrenia, which illustrated a successful application of the curve mapping in neuroimaging studies [32].

Comparison with Landmark Matching

The first purpose of this section is to compare the matched results of PT surfaces via the curve matching algorithm with those from the landmark matching algorithm. Twenty PTs were used in this experiment. As for the PT structure, three corner points and three boundary curves of the PT are defined as point and curve objects across the population. In the landmark matching process, five points equally spaced on each boundary and the three corner points were chosen as point landmarks on each PT surface. Then, the landmark

matching algorithm [18,42] was applied to PTs to obtain the deformation field that was used to deform PT surfaces to the template. Since the PT structure is relatively flat and simple compared with other structures of the brain, the cumulative distance distribution between deformed source and target surfaces, as described in the previous section, can be used as quantitative validation measurement. Figure 14 shows the averages for the original source surfaces (solid line), deformed ones via the landmark matching (dashdot line), and deformed ones via the curve matching (dash line). This figure suggests that the cumulative distance distribution from the curve matching algorithm is above that from the landmark matching algorithm, which implies that the curve matching algorithm introduced here significantly improves matching results in terms of the surface distance measurement compared to those from the landmark matching method.

The second aim of this section is to compare deformation fields of CG surfaces from the landmark and curve matching algorithms. Landmark matching methods have been used to map curves and surfaces by extracting a pair labeled point sets from the curves as landmarks. However, manually labeling landmarks is labor-intensive as well as highly variable, and landmark matching methods are sensitive to the labeling. Consequently, it may result in giving incorrect mapping. In this experiment, we give such an example to show matching results and deformation fields via both landmark [18,42] and curve matching methods under the LDDMM framework. In the landmark matching process, seventy two landmarks were selected from the six curves shown in panel (b) of Figure 10, twelve landmarks per curve [49]. After the landmark matching, the deformation field was interpolated for the other vertices on the CG. Figures 15 and 16 give examples what the deformation fields are from the landmark and curve matchings. Panels (a)-(d) in both figures respectively show the target, source,

deformed source CG surface after the landmark matching, and deformed source CG surface after the curve matching. Two red points are marked on the target surface in Figures 15(a) and 16(a). Compared to the positions of these two points on the source surface, the relative positions are changed after the landmark matching process, which can be observed in panel (f) on both figures (zoom in version of the column in the triangulated mesh format). However, we do not observe such a change in the curve matching shown in panels (g) of Figure 15 and 16. Thus, we conclude that the curve matching gives more proper deformation field due to incorporating the geometry information of the curves.

6 Conclusion

In this work we have proposed a mathematical framework in which both curves and their discrete samples are represented as vector-valued measures and embedded in a Hilbert space structure. Coupled with a model of deformations of the ambient space, we designed variational problems for curve matching takes convenient explicit formulations due to the use of the kernel of the Hilbert norm. We derived the case of the large deformations, given by integration of time-dependant vector fields. We also derived the case of the similitude transformation in Appendix B. We presented experiments for 2D and 3D curve mappings, and validated the accuracy of matching as well as demonstrated the behaviors of the curve mapping. Results indicate that the curve matching gives good matching and proper deformation fields compared to the landmark matching algorithm [18]. We also proposed to apply this technique for shape classification using the metric distances provided by the large deformation framework.

Appendix

A Gradient of E

As the first step, we compute the derivative of the dissimilarity measure between two sequences of points $(z_i)_{i=1}^n$ and $(y_j)_{j=1}^m$ with respect to $\mathbf{z}$, given in (19):

$$E = \|\mu_{\mathbf{z}} - \mu_{\mathbf{y}}\|^2_{W^*} = \sum_{i=1}^{n-1}\sum_{j=1}^{n-1}\Big[k_W(c_{\mathbf{z},i}, c_{\mathbf{z},j})\tau_{\mathbf{z},i}\Big]\cdot\tau_{\mathbf{z},j} - 2\sum_{i=1}^{n-1}\sum_{j=1}^{m-1}\Big[k_W(c_{\mathbf{z},i}, c_{\mathbf{y},j})\tau_{\mathbf{z},i}\Big]\cdot\tau_{\mathbf{y},j} + \sum_{i=1}^{m-1}\sum_{j=1}^{m-1}\Big[k_W(c_{\mathbf{y},i}, c_{\mathbf{y},j})\tau_{\mathbf{y},i}\Big]\cdot\tau_{\mathbf{y},j}\ .$$

Let $1 \leq q \leq n$ and $z_q + \varepsilon\tilde{z}_q$ be a small perturbation of point $z_q \in \mathbb{R}^d$, with other points fixed. Since $c_{\mathbf{z},i} = \frac{1}{2}(z_i + z_{i+1})$ and $\tau_{\mathbf{z},i} = z_{i+1} - z_i$, we have

$$\frac{\partial c_{\mathbf{z},i}}{\partial\varepsilon} = \begin{cases} \frac{1}{2}\tilde{z}_q \text{ if } i = q \text{ or } i = q-1 \\ 0 \text{ otherwise} \end{cases} \qquad \frac{\partial \tau_{\mathbf{z},i}}{\partial\varepsilon} = \begin{cases} \tilde{z}_q \text{ if } i = q-1 \\ -\tilde{z}_q \text{ if } i = q \\ 0 \text{ otherwise.} \end{cases}$$

We consider kernels of the form $k_W(x,y) = h(|x-y|^2)$ and we note $h_{\mathbf{x},\mathbf{y},i,j} = h(|c_{\mathbf{x},i} - c_{\mathbf{y},j}|^2) \in \mathbb{R}$ and $h'_{\mathbf{x},\mathbf{y},i,j} = \frac{\partial h(|c_{\mathbf{x},i}-c_{\mathbf{y},j}|^2)}{\partial c_{\mathbf{x},i}} = 2h'(|c_{\mathbf{x},i} - c_{\mathbf{y},j}|^2)(c_{\mathbf{x},i} - c_{\mathbf{y},j}) \in \mathbb{R}^d$ for any sequences of points

$\mathbf{x}, \mathbf{y}$ and indices i, j. We get

$$\begin{aligned}\frac{\partial E}{\partial \varepsilon} &= \sum_{j=1}^{n-1} \left(h'_{\mathbf{z},\mathbf{z},q,j} \cdot \tilde{z}_q\right)(\tau_{\mathbf{z},q} \cdot \tau_{\mathbf{z},j}) + \sum_{j=1}^{n-1} \left(h'_{\mathbf{z},\mathbf{z},q-1,j} \cdot \tilde{z}_q\right)(\tau_{\mathbf{z},q-1} \cdot \tau_{\mathbf{z},j}) \\ &\quad +2\sum_{j=1}^{n-1}(h_{\mathbf{z},\mathbf{z},q-1,j} - h_{\mathbf{z},\mathbf{z},q,j})(\tilde{z}_q \cdot \tau_{\mathbf{z},j}) - 2\sum_{j=1}^{n-1}(h_{\mathbf{z},\mathbf{y},q-1,j} - h_{\mathbf{z},\mathbf{y},q,j})(\tilde{z}_q \cdot \tau_{\mathbf{y},j}) \\ &\quad -\sum_{j=1}^{m-1} \left(h'_{\mathbf{z},\mathbf{y},q,j} \cdot \tilde{z}_q\right)(\tau_{\mathbf{z},q} \cdot \tau_{\mathbf{y},j}) - \sum_{j=1}^{m-1} \left(h'_{\mathbf{z},\mathbf{y},q-1,j} \cdot \tilde{z}_q\right)(\tau_{\mathbf{z},q-1} \cdot \tau_{\mathbf{y},j}).\end{aligned}$$

Hence the gradient of E with respect to $\mathbf{z}_q$ is given by

$$\begin{aligned}\nabla_{z_q} E &= \sum_{j=1}^{n-1}(\tau_{\mathbf{z},q} \cdot \tau_{\mathbf{z},j})h'_{\mathbf{z},\mathbf{z},q,j} + \sum_{j=1}^{n-1}(\tau_{\mathbf{z},q-1} \cdot \tau_{\mathbf{z},j})h'_{\mathbf{z},\mathbf{z},q-1,j} \\ &\quad +2\sum_{j=1}^{n-1}(h_{\mathbf{z},\mathbf{z},q-1,j} - h_{\mathbf{z},\mathbf{z},q,j})\tau_{\mathbf{z},j} - 2\sum_{j=1}^{n-1}(h_{\mathbf{z},\mathbf{y},q-1,j} - h_{\mathbf{z},\mathbf{y},q,j})\tau_{\mathbf{y},j} \\ &\quad -\sum_{j=1}^{m-1}(\tau_{\mathbf{z},q} \cdot \tau_{\mathbf{y},j})h'_{\mathbf{z},\mathbf{y},q,j} - \sum_{j=1}^{m-1}(\tau_{\mathbf{z},q-1} \cdot \tau_{\mathbf{y},j})h'_{\mathbf{z},\mathbf{y},q-1,j}.\end{aligned} \tag{19}$$

B Similarity Transformation

B.1 Quaternion Representation of Similitude Transformation

Here we set $d = 3$ and look at transformations of the form $\phi(x) = Rx + \mathbf{b}$, where R is a similitude matrix defined by the direct product of uniform scale with orthogonal spatial rotation and $\mathbf{b}$ is a translation vector. The algebra of quaternions is a useful mathematical tool for formulating the composition of arbitrary spatial rotations, and establishing the

correctness of algorithms founded upon such compositions. Here, we use the quaternion $\mathbf{q} = [\mathbf{a}, s]$ to represent a similitude transformation, where $\mathbf{a}$ is a vector with three entries a_1, a_2, a_3 to describe spatial rotation and s is a scalar. We do not restrict the length of $\mathbf{q}$ to 1 so that the scaling factor is also considered.

The group $(Q, \circ)$ is defined as the set of quaternions Q with the law of composition $\circ$: $Q \times Q \to Q$, given by

$$\mathbf{q}_1 \circ \mathbf{q}_2 = [\mathbf{a}_1 \times \mathbf{a}_2 + s_1\mathbf{a}_2 + s_2\mathbf{a}_1, s_1 s_2 - \mathbf{a}_1 \cdot \mathbf{a}_2] \ . \tag{20}$$

The inverse of $\mathbf{q}$ is $\mathbf{q}^{-1} = \frac{1}{s^2 + \mathbf{a}\cdot\mathbf{a}}\mathbf{q}^*$, where $\mathbf{q}^*$ is the conjugate of $\mathbf{q}$ defined as $\mathbf{q}^* = [-\mathbf{a}, s]$. According to the law of composition in (20), the similitude operation R on $x \in \mathbb{R}^3$ is described as $[Rx, 0] = \mathbf{q} \circ [x, 0] \circ \mathbf{q}^*$, where

$$Rx = 2s\mathbf{a} \times x + 2(\mathbf{a} \cdot x)\mathbf{a} + (s^2 - |\mathbf{a}|^2)x \ . \tag{21}$$

B.2 Similarity alignment of curves

In the continuous setting, the alignment of two curves C and S is performed through minimization of the following functional:

$$J(s, \mathbf{a}, \mathbf{b}) = E(\phi(C), S) = \left\| \mu_{\phi(C)} - \mu_S \right\|^2_{W^*} ,$$

where $\phi(x) = Rx + \mathbf{b}$, with R parametrized by variables s and $\mathbf{a}$ via formula (21). When curves C and S are discretized via sequences $\mathbf{x} = (x_i)_{i=1}^n$ and $\mathbf{y} = (y_j)_{j=1}^m$, we consider the

functional

$$J(s, \mathbf{a}, \mathbf{b}) = E(\mathbf{z}, \mathbf{y}) = \left\| \sum_{i=1}^{n} \tau_{\mathbf{z},i} \delta_{c_{\mathbf{z},i}} - \sum_{j=1}^{m} \tau_{\mathbf{y},j} \delta_{c_{\mathbf{y},j}} \right\|_{W^*}^2 ,$$

where $z_i = Rx_i + \mathbf{b}$. The derivative of this functional is computed in appendix C.

C Gradient of a matching functional with respect to parameters of similarity transformations

We need to compute the gradient of a dissimilarity functional

$$J(s, \mathbf{a}, \mathbf{b}) = E(\mathbf{z}, \mathbf{y}),$$

where $\mathbf{z} = (z_i)_{i=1}^n = (\phi(x_i))_{i=1}^n$ and $\phi(x) = Rx + \mathbf{b}$, R computed from parameters s and $\mathbf{a}$ via formula (21): $Rx = 2s\mathbf{a} \times x + 2(\mathbf{a} \cdot x)\mathbf{a} + (s^2 - |\mathbf{a}|^2)x$. Let first compute the gradient of J with respect to parameter s. We have

$$\nabla_s J = \sum_{i=1}^{n} \frac{\partial \phi(x_i)}{\partial s} \cdot \nabla_{\phi(x_i)} E = \sum_{i=1}^{n} (2sx_i + 2\mathbf{a} \times x_i) \cdot \nabla_{\phi(x_i)} E \ . \tag{22}$$

The gradient of J with respect to parameters $\mathbf{a}$ can be computed as follows. Let $\mathbf{a}_\varepsilon =$

$\mathbf{a} + \varepsilon\tilde{\mathbf{a}}$ and take derivatives at $\varepsilon = 0$. We have

$$\begin{aligned}
\partial_\varepsilon J &= \sum_{i=1}^{n} \partial_\varepsilon(\phi(x_i)) \cdot \nabla_{\phi(x_i)} E \\
&= \sum_{i=1}^{n} -2(\mathbf{a}\cdot\tilde{\mathbf{a}})(x_i \cdot \nabla_{\phi(x_i)} E) + 2s(\tilde{\mathbf{a}} \times x_i) \cdot \nabla_{\phi(x_i)} E + \\
&\quad 2(\tilde{\mathbf{a}} \cdot x_i)(\mathbf{a} \cdot \nabla_{\phi(x_i)} E) + 2(\mathbf{a} \cdot x_i)(\tilde{\mathbf{a}} \cdot \nabla_{\phi(x_i)} E) \ .
\end{aligned}$$

Since $(\tilde{\mathbf{a}} \times x_i) \cdot \nabla_{\phi(x_i)} E = (x_i \times \nabla_{\phi(x_i)} E) \cdot \tilde{\mathbf{a}}$, we obtain

$$\partial_\varepsilon J = \sum_{i=1}^{n} \tilde{\mathbf{a}} \cdot [-2(x_i \cdot \nabla_{\phi(x_i)} E)\mathbf{a} + 2s(x_i \times \nabla_{\phi(x_i)} E) + 2(\mathbf{a} \cdot \nabla_{\phi(x_i)} E)x_i + 2(\mathbf{a} \cdot x_i)\nabla_{\phi(x_i)} E)] \ .$$

The first and third terms form a double wedge product: $-(x_i \cdot \nabla_{\phi(x_i)} E)\mathbf{a} + (\mathbf{a} \cdot \nabla_{\phi(x_i)} E)x_i = (\mathbf{a} \times x_i) \times \nabla_{\phi(x_i)} E$ so finally the gradient is

$$\nabla_{\mathbf{a}} J = \sum_{i=1}^{n} 2(\mathbf{a} \times x_i) \times \nabla_{\phi(x_i)} E + 2s(x_i \times \nabla_{\phi(x_i)} E) + 2(\mathbf{a} \cdot x_i)\nabla_{\phi(x_i)} E \ . \tag{23}$$

We can compute the derivative of the gradient of J with respect to translation $\mathbf{b}$ in the same way as for $\mathbf{s}$ and get

$$\nabla_{\mathbf{b}} J = \sum_{i=1}^{n} \nabla_{\phi(x_i)} E \ . \tag{24}$$

The gradients with respect to s, $\mathbf{a}$, and $\mathbf{b}$ in (22, 23, 24) all involve the term $\nabla_{\phi(x_i)} E$ given in (19) (with $z_i = \phi(x_i)$).

D Gradient of a point-based matching functional in the large deformation setting

We rewrite J into a matrix form

$$J = \gamma \int_0^1 \boldsymbol{\alpha}_t \cdot k_V(\mathbf{x_t}, \mathbf{x_t})\boldsymbol{\alpha}_t + E(\mathbf{x}_1, \mathbf{y}) \ , \tag{25}$$

where $\boldsymbol{\alpha}_t$ and $\mathbf{x_t}$ are vectors of momentum and coordinates of vertices at time t. E denotes the matching functional.

Lemma 2. *The gradient of J with respect to momentum $\boldsymbol{\alpha}_t$ with metric given by matrix $k_V(\mathbf{x}_t, \mathbf{x}_t)$ at time t is of the form $(\nabla J)_t = 2\gamma\boldsymbol{\alpha}_t + \eta_t$, where vector $\eta_t = \nabla_{\mathbf{x}_1} E + \int_t^1 (\partial_{\mathbf{x}_s}[k_V(\mathbf{x}_s, \mathbf{x}_s)\boldsymbol{\alpha}_s])^*(\eta_s + \gamma\boldsymbol{\alpha}_s)ds$ and $\nabla_{\mathbf{x}_1} E$ is given in (19).*

Proof. Our first goal is to compute variation of velocity fields v_t and trajectories $\mathbf{x}_t$ given a variation $\boldsymbol{\alpha}^\epsilon = \boldsymbol{\alpha} + \epsilon\tilde{\boldsymbol{\alpha}}$.

We have

$$v_t(x) = \sum_{k=1}^{N} k_V(x_k(t), x)\alpha_k(t) = k_V(\mathbf{x}_t, x)\boldsymbol{\alpha}_t \ , \text{ and} \tag{26}$$

$$\mathbf{x}_t = \mathbf{x} + \int_0^t k_V(\mathbf{x}_s, \mathbf{x}_s)\boldsymbol{\alpha}_s ds \ . \tag{27}$$

For a variation $\boldsymbol{\alpha}^\epsilon = \boldsymbol{\alpha} + \epsilon\tilde{\boldsymbol{\alpha}}$, computing the derivative with respect to ϵ in (26) yields the corresponding variation of velocity field $\tilde{v} = \partial_\epsilon v^\epsilon$ as the form

$$\tilde{v}_t(x) = \partial_{\mathbf{x}_t}[k_V(\mathbf{x}_t, x)\boldsymbol{\alpha}_t]\tilde{\mathbf{x}}_t + k_V(\mathbf{x}_t, x)\tilde{\boldsymbol{\alpha}}_t \ ,$$

where ∂_i is the derivative with respect to the ith variable in k_V. Similarly, the corresponding variation of trajectory $\tilde{\mathbf{x}}_t = \partial_\epsilon \phi_t^{v^\epsilon}(\mathbf{x})$ from (15) is of the form

$$\tilde{\mathbf{x}}_t = \int_0^t \partial_{\mathbf{x}_s}[k_V(\mathbf{x}_s, \mathbf{x}_s)\boldsymbol{\alpha}_s]\tilde{\mathbf{x}}_s + k_V(\mathbf{x}_s, \mathbf{x}_s)\tilde{\boldsymbol{\alpha}}_s ds \ .$$

To obtain $\tilde{\mathbf{x}}_t$ a manipulation is needed. The above equation can be rewritten as

$$\frac{d\tilde{\mathbf{x}}_t}{dt} = \partial_{\mathbf{x}_t}[k_V(\mathbf{x}_t, \mathbf{x}_t)\boldsymbol{\alpha}_t]\tilde{\mathbf{x}}_t + k_V(\mathbf{x}_t, \mathbf{x}_t)\tilde{\boldsymbol{\alpha}}_t \ ,$$

which is a linear differential equation in variable $\tilde{\mathbf{x}}_t$. By the variation of constants method, we are able to write the solution of $\tilde{\mathbf{x}}_t$ as

$$\tilde{\mathbf{x}}_t = \int_0^t R_{st} k_V(\mathbf{x}_s, \mathbf{x}_s)\tilde{\boldsymbol{\alpha}}_s ds \ ,$$

where operator R_{st} gives the solution of the homogeneous equation

$$\frac{dR_{st}}{dt} = \partial_{\mathbf{x}_t}[k_V(\mathbf{x}_t, \mathbf{x}_t)\boldsymbol{\alpha}_t]R_{st} \ .$$

It remains to express the variation of the energy $\partial_\epsilon J$ in the form

$$\partial_\epsilon J = 2\gamma \int_0^1 \tilde{\boldsymbol{\alpha}}_t \cdot k_V(\mathbf{x}_t, \mathbf{x}_t)\boldsymbol{\alpha}_t dt + \gamma \int_0^1 \boldsymbol{\alpha}_t \cdot \partial_\epsilon(k_V(\mathbf{x}_t^\epsilon, \mathbf{x}_t^\epsilon)\boldsymbol{\alpha}_t)dt + d_{\mathbf{x}_1} E \partial_\epsilon(\mathbf{x}_1^\epsilon) \ .$$

Substituting $\tilde{v}_t(x)$ and $\tilde{\mathbf{x}}_t$ in $\partial_\epsilon J$, we have the second term as

$$\int_0^1 \boldsymbol{\alpha}_t \cdot \partial_\epsilon (k_V(\mathbf{x}_t^\epsilon, \mathbf{x}_t^\epsilon)\boldsymbol{\alpha}_t) dt = \int_0^1 \big(\int_t^1 R_{ts}^* \partial_{\mathbf{x}_s} [k_V(\mathbf{x}_s, \mathbf{x}_s)\boldsymbol{\alpha}_s]^* ds \big) \cdot k_V(\mathbf{x}_t, \mathbf{x}_t)\tilde{\boldsymbol{\alpha}}_t dt \ .$$

The third term can be rewritten as

$$d_{\mathbf{x}_1} E \partial_\epsilon (\mathbf{x}_1^\epsilon) = \int_0^1 d_{\mathbf{x}_1} E R_{t1} k_V(\mathbf{x}_t, \mathbf{x}_t)\tilde{\boldsymbol{\alpha}}_t dt \ .$$

We finally obtain

$$\partial_\epsilon J = \int_0^1 k_V(\mathbf{x}_t, \mathbf{x}_t)\big(2\gamma\boldsymbol{\alpha}_t + \eta_t\big) \cdot \tilde{\boldsymbol{\alpha}}_t dt \ .$$

The gradient $\nabla J \in L^2([0,1], (\mathbb{R}^d)^n)$ at time t is given

$$(\nabla J)_t = k_V(\mathbf{x}_t, \mathbf{x}_t)\big(2\gamma\boldsymbol{\alpha}_t + \eta_t\big) \ .$$

Vector $\eta_t = \gamma \int_0^1 R_{ts}^* \partial_{\mathbf{x}_s} [k_V(\mathbf{x}_s, \mathbf{x}_s)\boldsymbol{\alpha}_s]^* ds + R_{t1}^* \nabla_{\mathbf{x}_1} E$ and it can be written in the backward integral equation

$$\eta_t = \nabla_{\mathbf{x}_1} E + \int_t^1 (\partial_{\mathbf{x}_s} [k_V(\mathbf{x}_s, \mathbf{x}_s)\boldsymbol{\alpha}_s])^* (\eta_s + \gamma\boldsymbol{\alpha}_s) ds \ . \tag{28}$$

The choice of the metric over momentum $\boldsymbol{\alpha}_t$ in the space of L^2 is arbitrary. A reasonable choice of metric is given by $k_V(\mathbf{x}_t, \mathbf{x}_t)$ with two-fold advantages of being closer to the metric inducing the space of velocity field v and simplifying the formula for the gradient. Therefore,

the gradient $(\nabla J)_t$ can be simplified as

$$(\nabla J)_t = 2\gamma \boldsymbol{\alpha}_t + \eta_t \ .$$

□

Acknowledgements

The work reported here was supported by grants: NIH P41 RR15241, NSF DMS 0456253, and National University of Singapore start-up grant R-397-000-058-133.

References

[1] Z. Zhang, "Iterative point matching for registration of free-form curves and surfaces," *International Journal of Computer Vision*, vol. 13(2), pp. 119–152.

[2] P. Besl and N. McKay, "A method for registration of 3-d shapes," *IEEE Transactions on Pattern Analysis and Machine Intelligence*, vol. 14(2), pp. 239–256, February 1992.

[3] J. Feldmar and N. Ayache, "Rigid, affine and locally affine registration of free-form surfaces," vol. 18(2), pp. 99–119, May 1996.

[4] W. Welker, "Why does cerebral cortex fissure and fold?" *Cereb Cortex*, vol. 83, pp. 3–136, 1990.

[5] S. Durrleman, X. Pennec, A. Trouve, and N. Ayache, "Measuring brain variability via sulcal lines registration: a diffeomorphic approach," *Int Conf Med Image Comput Comput Assist Interv*, pp. 675–682, 2007.

[6] P. Fillard, V. Arsigny, X. Pennec, K. Hayashi, P. Thompson, and N. Ayache, "Measuring brain variability by extrapolating sparse tensor fields measured on sulcal lines," *Neuroimage*, vol. 34, pp. 639–650, 2007.

[7] P. M. Thompson, C. Schwartz, R. T. Lin, A. A. Khan, and A. W. Toga, "Three–dimensional statistical analysis of sulcal variability in the human brain," *J. Neurosci.*, vol. 16, no. 13, pp. 4261–4274, 1996.

[8] M. E. Rettmann, X. Han, C. Xu, and J. L. Prince, "Automated sulcal segmentation using watersheds on the cortical surface," *NeuroImage*, vol. 15, no. 2, pp. 329–44, 2002.

[9] U. Grenander and M. I. Miller, "Computational anatomy: An emerging discipline," *Quarterly of Applied Mathematics*, vol. 56, no. 4, pp. 617–694, 1998.

[10] J. C. Gee and R. K. Bajcsy, "Elastic matching: Continuum mechanical and probabilistic analysis," in *Brain Warping*, A. W. Toga, Ed. San Diego: Academic Press, 1999, pp. 183–196.

[11] M. I. Miller, A. Trouvé, and L. Younes, "On the metrics and Euler-Lagrange equations of computational anatomy," *Annual Review of Biomedical Engineering*, vol. 4, pp. 375–405, 2002.

[12] C. Twining, S. Marsland, and C. Taylor, "Measuring geodesic distances on the space of bounded diffeomorphisms," in *Proceedings of the British Machine Vision Conference (BMVC), Cardiff, September 2002*, vol. 2, 2002, pp. 847–856.

[13] M. F. Beg, M. I. Miller, A. Trouvé, and L. Younes, "Computing large deformation metric mappings via geodesic flows of diffeomorphisms," *International Journal of Computer Vision*, vol. 61, no. 2, pp. 139–157, February 2005.

[14] S. C. Joshi, B. Davis, M. Jomier, and G. Gerig, "Unbiased diffeomorphic atlas construction for computational anatomy," *NeuroImage*, vol. 23, pp. 151–160, 2004.

[15] B. Avants and J. C. Gee, "Geodesic estimation for large deformation anatomical shape and intensity averaging," *NeuroImage*, vol. 23, pp. 139–150, 2004.

[16] P. Thompson and A. Toga, "A surface-based technique for warping three-dimensional image of the brain," *IEEE Trans. Med. Imag.*, vol. 15, no. 4, 1996.

[17] P. M. Thompson, K. M. Hayashi, E. R. Sowell, N. Gogtay, J. N. Giedd, J. L. Rapoport, G. I. de Zubicaray, A. L. Janke, S. E. Rose, J. Semple, D. M. Doddrell, Y. Wang, T. G. van Erp, T. D. Cannon, and A. W. Toga, "Mapping cortical change in alzheimer's disease, brain development, and schizophrenia," *NeuroImage*, vol. 23, pp. S2–S18, 2004.

[18] S. C. Joshi and M. I. Miller, "Landmark matching via large deformation diffeomorphisms," *IEEE Trans. Image Processing*, vol. 9, no. 8, pp. 1357–1370, 2000.

[19] V. Camion and L. Younes, "Geodesic interpolating splines," in *EMMCVPR 2001*, ser. Lecture notes in computer sciences, M. Figueiredo, J. Zerubia, and K. Jain, A, Eds., vol. 2134. Springer, 2001.

[20] P. A. Helm, L. Younes, M. F. Beg, D. B. Ennis, C. Leclercq, O. P. Faris, E. McVeigh, D. Kass, M. I. Miller, and R. L. Winslow, "Evidence of structural remodeling in the dyssynchronous failing heart," *Circ. Res.*, vol. 98, pp. 125 – 132, 2006.

[21] A. Trouvé, "An infinite dimensional group approach for physics based models," 1995, technical report (electronically available at http://www.cis.jhu.edu).

[22] P. Dupuis, U. Grenander, and M. I. Miller, "Variational problems on flows of diffeomorphisms for image matching," *Quaterly of Applied Math.*, vol. 56, pp. 587–600, 1998.

[23] M. F. Beg, "Variational and computational methods for flows of diffeomorphisms in image matching and growth in computational anatomy," Ph.D. dissertation, Johns Hopkins University, 2003.

[24] Y. Cao, M. Miller, R. Winslow, and L. Younes, "Large deformation diffeomorphic metric mapping of vector fields," *IEEE Trans. Med. Imag.*, vol. 24, pp. 1216–1230, 2005.

[25] Y. Cao, M. I. Miller, R. L. Winslow, and L. Younes, "Large deformation diffeomorphic metric mapping of fiber orientations," in *ICCV*. Beijing, China: IEEE Computer Society, October 2005, pp. 1379–1386.

[26] A. A. Joshi, D. W. Shattuck, P. M. Thompson, and R. M. Leahy, "Registration of cortical surfaces using sulcal landmarks for group analysis of meg data," in *International Congress Series Volume 1300, , New Frontiers in Biomagnetism. Proceedings of the 15th International Conference on Biomagnetism, Vancouver, BC, Canada, August 21-25, 2006*, June 2007, pp. 229–232.

[27] M. Bakircioglu, S. Joshi, and M. Miller, "Landmark matching on brain surfaces via large deformation diffeomorphisms on the sphere," in *Proc. SPIE Medical Imaging 1999: Image Processing*, vol. 3661, San Diego, CA, February 1999, pp. 710–715.

[28] A. Leow, P. M. Thompson, H. Protas, and S.-C. Huang, "Brain warping with implicit representations," in *ISBI*. IEEE, 2004, pp. 603–606.

[29] J. Glaunès, A. Trouvé, and L. Younes, "Diffeomorphic matching of distributions: A new approach for unlabelled point-sets and sub-manifolds matching." CVPR, IEEE Computer Society, 2004, pp. 712–718.

[30] M. Vaillant and J. Glaunès, "Surface matching via currents," *Lecture Notes in Comp. Sci.: Inform. Proc. in Med. Imaging*, vol. 3565, pp. 381–392, 2005.

[31] J. Glaunès, A. Trouvé, and L. Younes, "Modeling planar shape variation via hamiltonian flows of curves," in *Statistics and Analysis of Shapes*, H. Krim and A. Yezzi, Eds. Birkhauser, may 2006.

[32] A. Qiu, L. Younes, L. Wang, J. T. Ratnanather, S. K. Gillepsie, G. Kaplan, J. G. Csernansky, and M. I. Miller, "Combining anatomical manifold information via diffeomorphic metric mappings for studying cortical thinning of the cingulate gyrus in schizophrenia," *Neuroimage*, vol. 37, pp. 821–833, 2007.

[33] E. Sharon and D. Mumford, "2d-shape analysis using conformal mapping," *International Journal of Computer Vision*, vol. 70, no. 1, pp. 55–75, 2006.

[34] L. Younes, "Computable elastic distances between shapes," *SIAM J. Applied Math.*, vol. 58, pp. 565–586, 1998.

[35] E. Klassen, A. Srivastava, W. Mio, and S. H. Joshi, "Analysis of planar shapes using geodesic paths on shape spaces," *IEEE Trans. Pattern Anal. Mach. Intell.*, vol. 26, no. 3, pp. 372–383, 2003.

[36] W. Mio and A. Srivastava, "Elastic-string models for representation and analysis of planar shapes," in *CVPR (2)*, 2004, pp. 10–15.

[37] F. R. Schmidt, M. Clausen, and D. Cremers, "Shape matching by variational computation of geodesics on a manifold," in *DAGM-Symposium*, ser. Lecture Notes in Computer Science, K. Franke, K.-R. Müller, B. Nickolay, and R. Schäfer, Eds., vol. 4174. Springer, 2006, pp. 142–151.

[38] P. W. Michor and D. Mumford, "An overview of the Riemannian metrics on spaces of curves using the Hamiltonian approach," *Appl. Comput. Harmon. Anal.*, vol. 23, no. 1, pp. 74–113, 2007.

[39] R. I. McLachlan and S. Marsland, "N-particle dynamics of the Euler equations for planar diffeomorphisms," *Dyn. Syst.*, vol. 22, no. 3, pp. 269–290, 2007.

[40] J. Glaunès, "Transport par difféomorphismes de points, de mesures et de courants pour la comparaison de formes etl l'anatomie numérique," Ph.D. dissertation, Université Paris 13, 2005.

[41] C. Yang, R. Duraiswami, N. Gumerov, and L. Davis, "Improved fast gauss transform and efficient kernel density estimation," *IEEE International Conference on Computer Vision*, pp. 464–471, 2003.

[42] S. Allassonnière, A. Trouvé, and L. Younes, "Geodesic shooting and diffeomorphic matching via textured meshes." in *EMMCVPR*, 2005, pp. 365–381.

[43] M. F. Cox and M. A. A. Cox, *Multidimensional Scaling.* Chapman and Hall, 2001.

[44] M. Joshi, J. Cui, K. Doolittle, S. Joshi, D. Van Essen, L. Wang, and M. I. Miller, "Brain segmentation and the generation of cortical surfaces," *NeuroImage*, vol. 9, pp. 461–476, 1999.

[45] M. I. Miller, A. B. Massie, J. T. Ratnanather, K. N. Botteron, and J. G. Csernansky, "Bayesian construction of geometrically based cortical thickness metrics," *NeuroImage*, vol. 12, pp. 676–687, 2000.

[46] X. Han, C. Xu, and J. L. Prince, "A topology preserving deformable model using level set," in *CVPR'2001*, vol. 2. Kauai, HI: IEEE, 2001, pp. 765–770.

[47] X. Han, C. Xu, U. Braga-Neto, and J. Prince, "Topology correction in brain cortex segmentation using a multiscale, graph-based algorithm," *IEEE Trans. Med. Imag.*, vol. 21, pp. 109–121, 2002.

[48] J. T. Ratnanather, P. E. Barta, N. A. Honeycutt, N. Lee, N. G. Morris, A. C. Dziorny, M. K. Hurdal, G. D. Pearlson, and M. I. Miller, "Dynamic programming generation of boundaries of local coordinatized submanifolds in the neocortex: application to the planum temporale," *NeuroImage*, vol. 20, no. 1, pp. 359–377, 2003.

[49] M. Bakircioglu, U. Grenander, N. Khaneja, and M. I. Miller, "Curve matching on brain surfaces using frenet distances," *Human Brain Mapping*, vol. 6, no. 5-6, pp. 329–333, 1998.

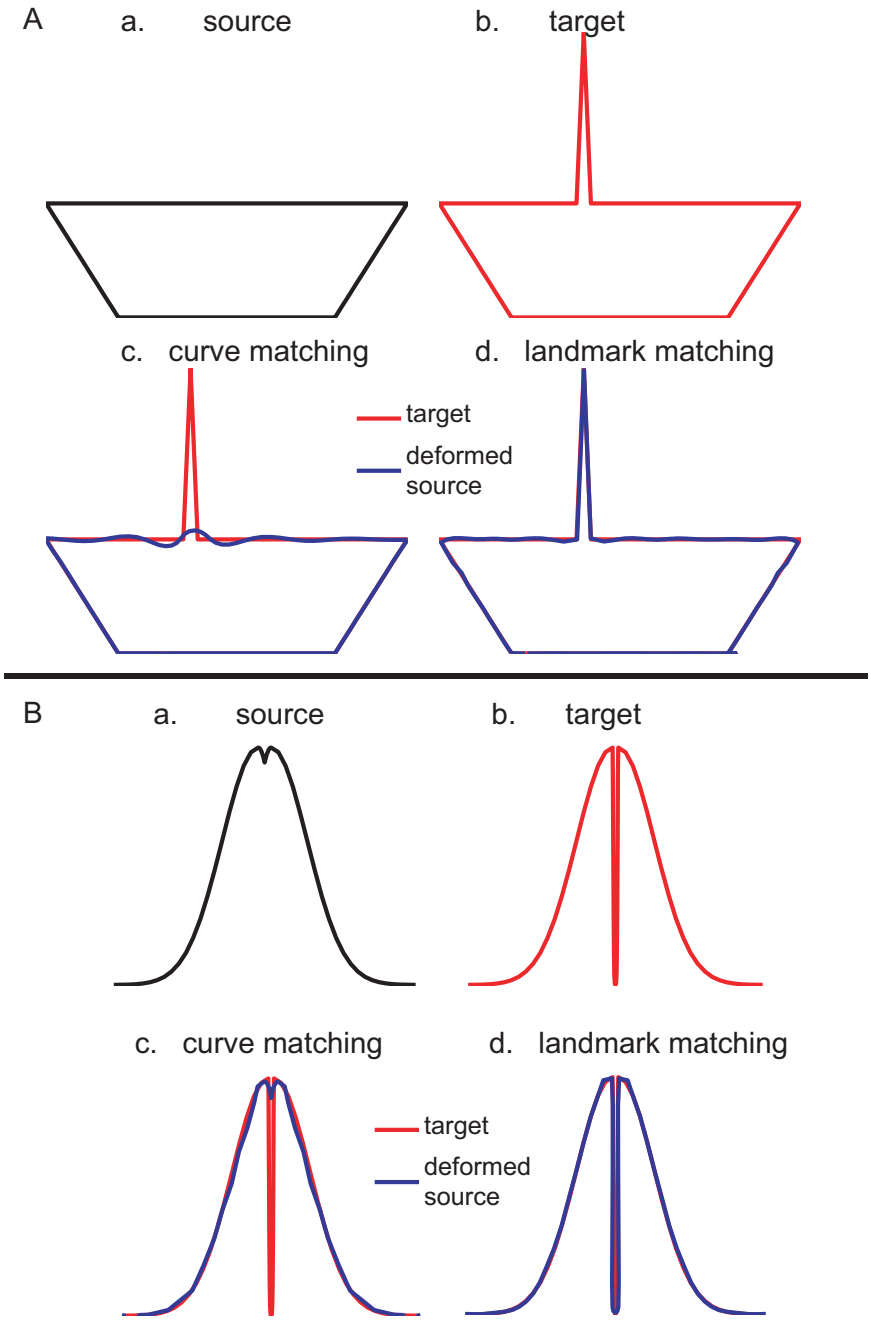

Figure 5: Comparison between the landmark and curve matchings. In each example (A) or (B), panels (a,b) show the source and target curves. Panels (c,d) show results from the curve and landmark matchings, respectively. The target and the deformed source shapes are respectively shown in red and blue.

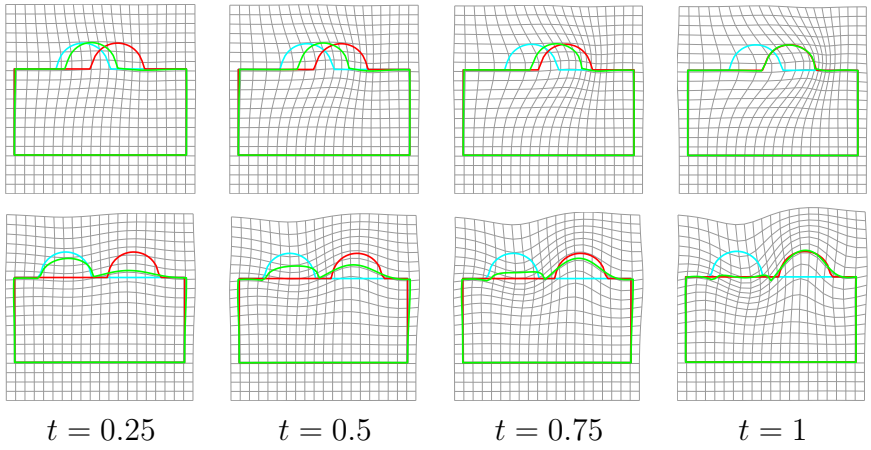

Figure 6: Box bump experiments. Each row shows one mapping from a template (cyan curve) to a target (red curve) with evolution of $\phi_t^{\hat{v}}$ at different times $t \in [0, 1]$ denoted by green curves. Top row: first experiment when two bumps on the template and target curves are close to each othter. Bottom row: second experiment when two bumps on the template and target curves are further from each other.

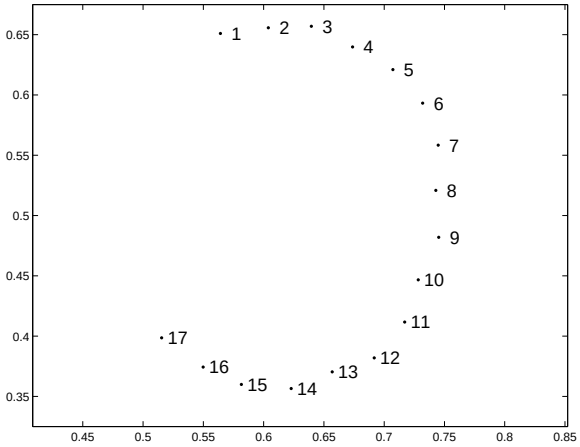

Figure 7: 2-dimensional scaling plot of the distance matrix computed from pairwise matchings of 17 box bumps shapes

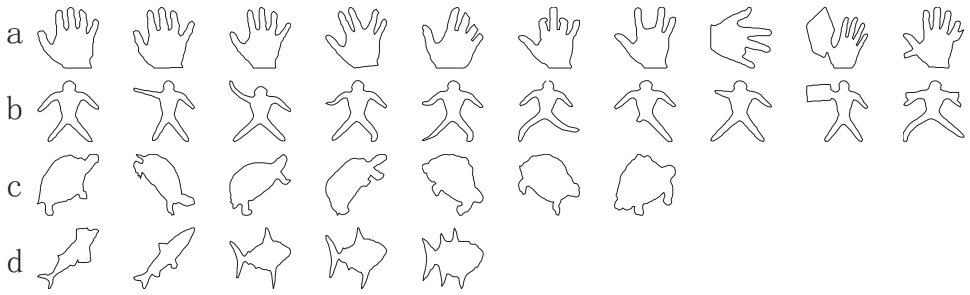

Figure 8: Rows (a-d) respectively show hand, dude, turtle, and fish.

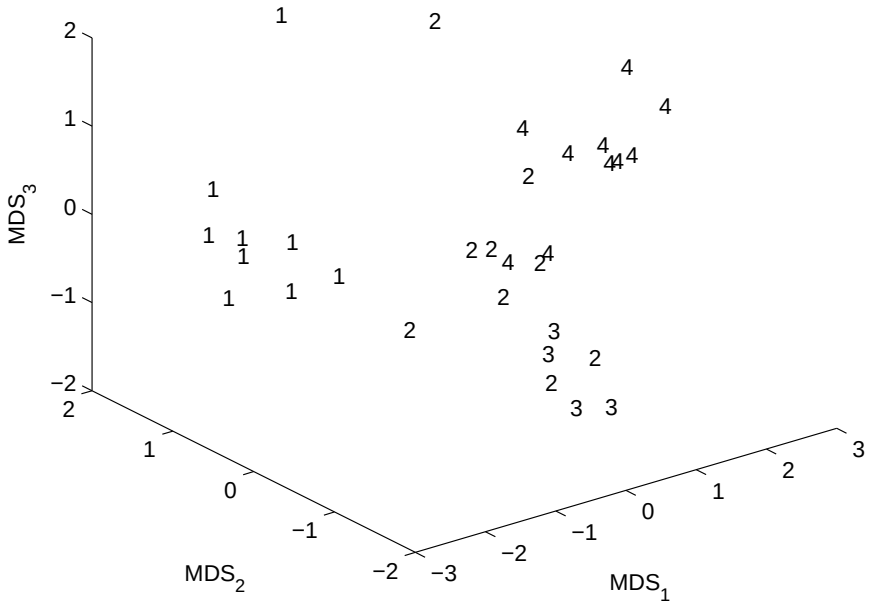

Figure 9: A scatter plot of feature dimensions from multidimensional scaling. 1:hand, 2:turtle, 3:fish, 4:dude.

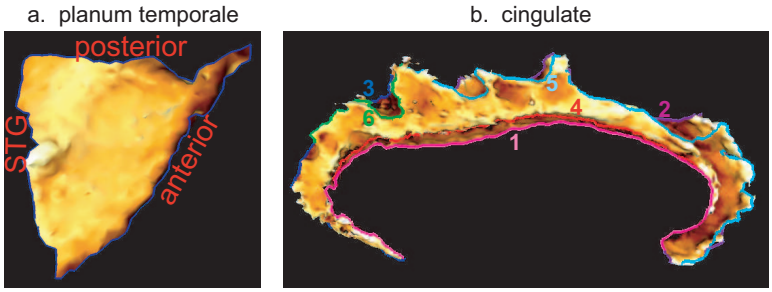

Figure 10: Panel (a) shows the curve defined as boundary curve for planum temporale cortical surface. Panel (b) depicts six curves describing the main shape of cingulate gyrus. Each curve is colored differently with indices in the same color scheme. The surfaces are colored by the curvature information

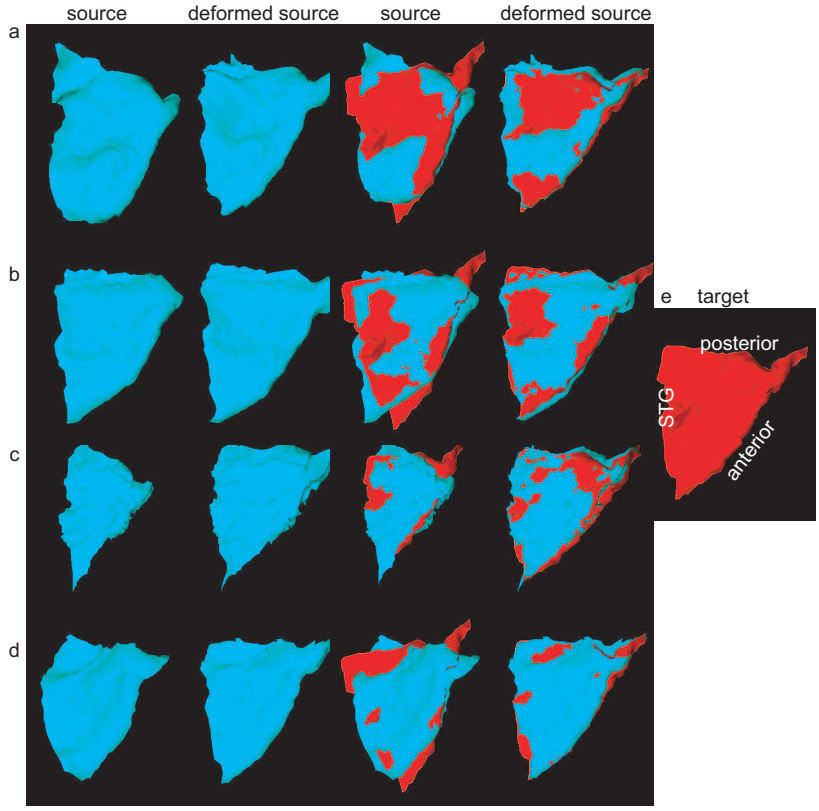

Figure 11: Three-dimensional deformation of planum temporale cortical surface. Panels (a)-(d) depict the deformation applied to planum temporale cortical surfaces. From the left to the right, panels respectively show the source and deformed source surfaces as well as the source and deformed source surfaces overlaying with the target surface in red. Panel (e) shows the target of planum temporale surface.

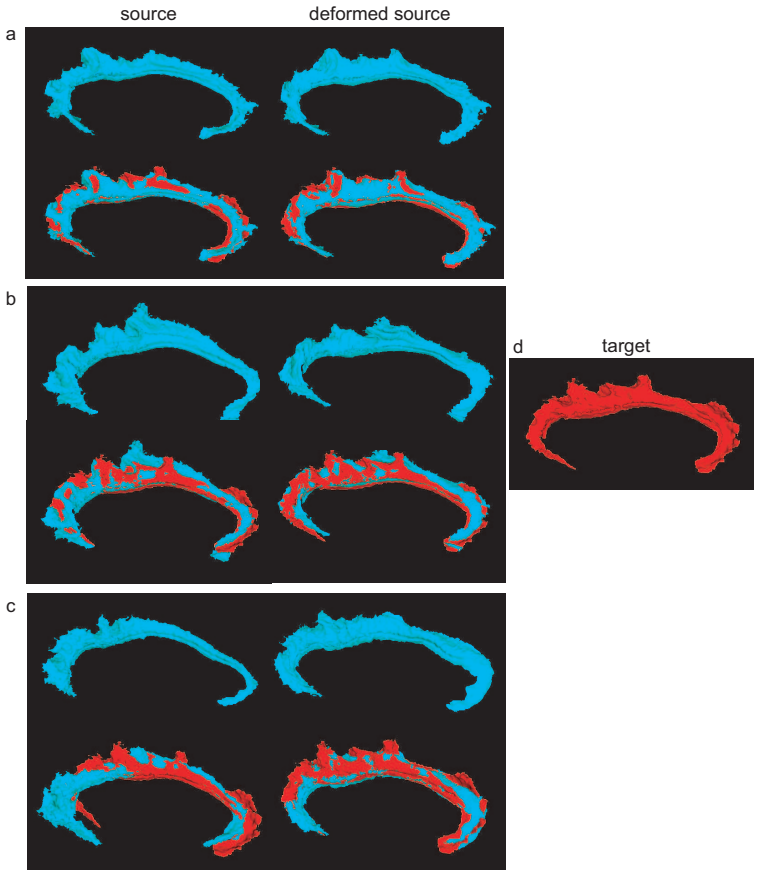

Figure 12: Three-dimensional deformation of cingulate cortical surface. Panels (a)-(c) depict the deformation applied to cingulate cortical surfaces. In each panel, the top row respectively shows the source and deformed source surfaces from the left to the right; the bottom shows the source and deformed source surfaces overlaying with the target surface in red, which is shown on panel (d).

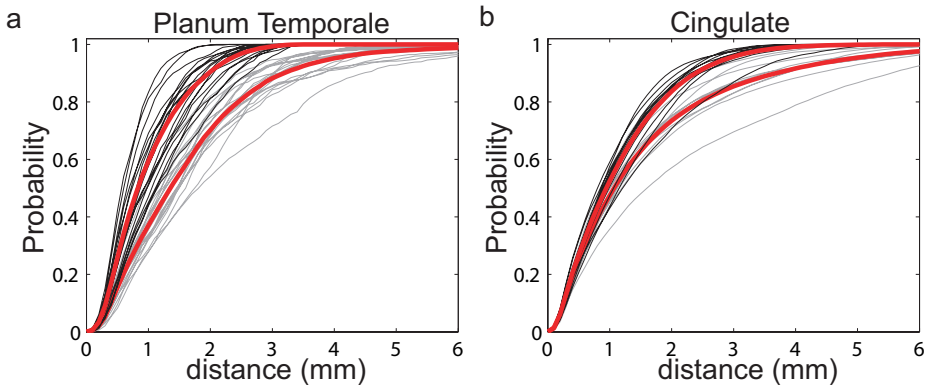

Figure 13: Panels (a) and (b) depict the cumulative distance distributions for planum temporale and cingulate surfaces. The cumulative distance distributions for the source surfaces are in gray, while the distributions for the deformed source surface are in black. Red curves are the mean distributions for the source and deformed source surfaces.

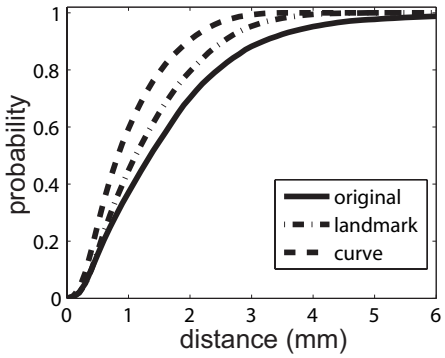

Figure 14: Comparison of the cumulative distance distributions between the landmark and curve matchings. Solid, dashdot, and dash lines represent average cumulative distance distributions over the original source, deformed source surfaces via the landmark and curve matchings, respectively.

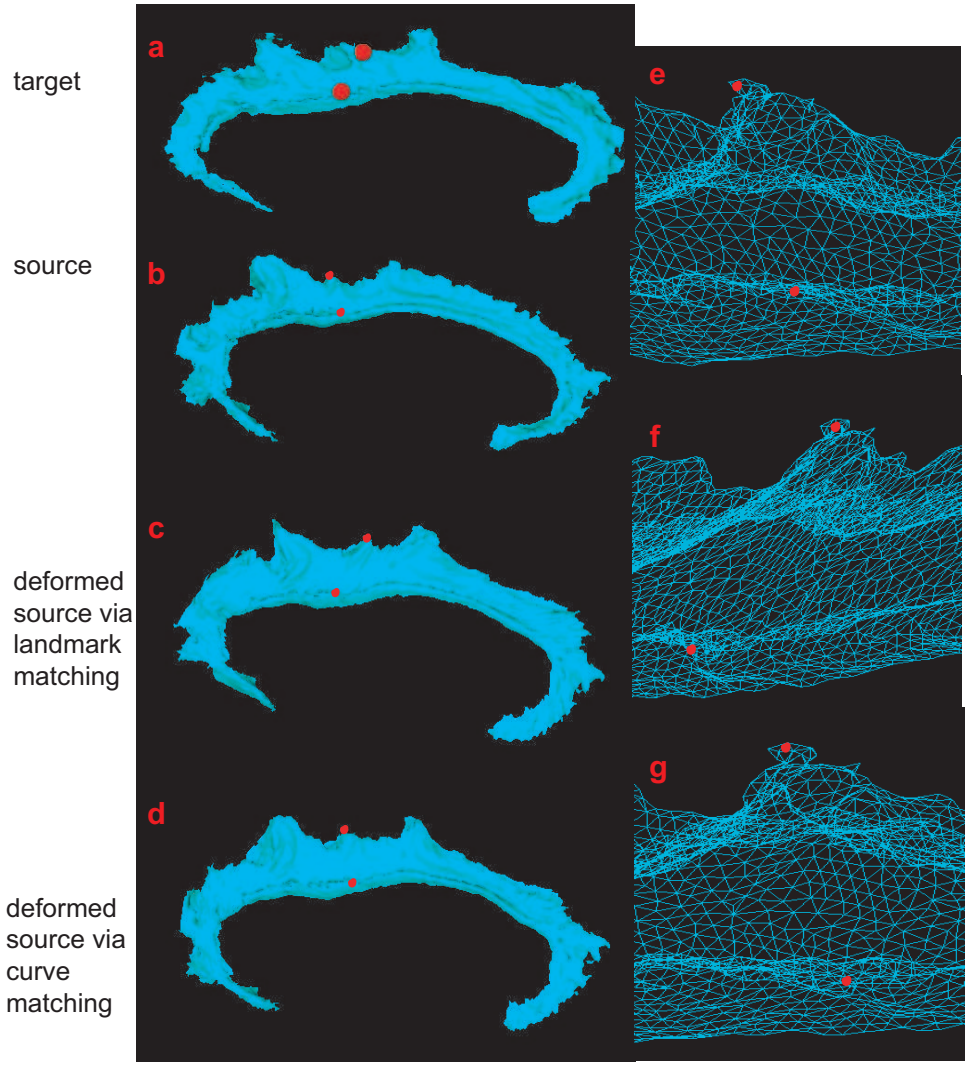

Figure 15: Comparison of deformation fields between the landmark and curve matchings. Panels (a-d) show the target, source, deformed source surface after the landmark matching, deformed source surface after the curve matching. Red dots represents paired landmarks on the target and source surfaces. Panels (e-g) show triangulated meshes respectively corresponding to the surfaces in panels (b-d).

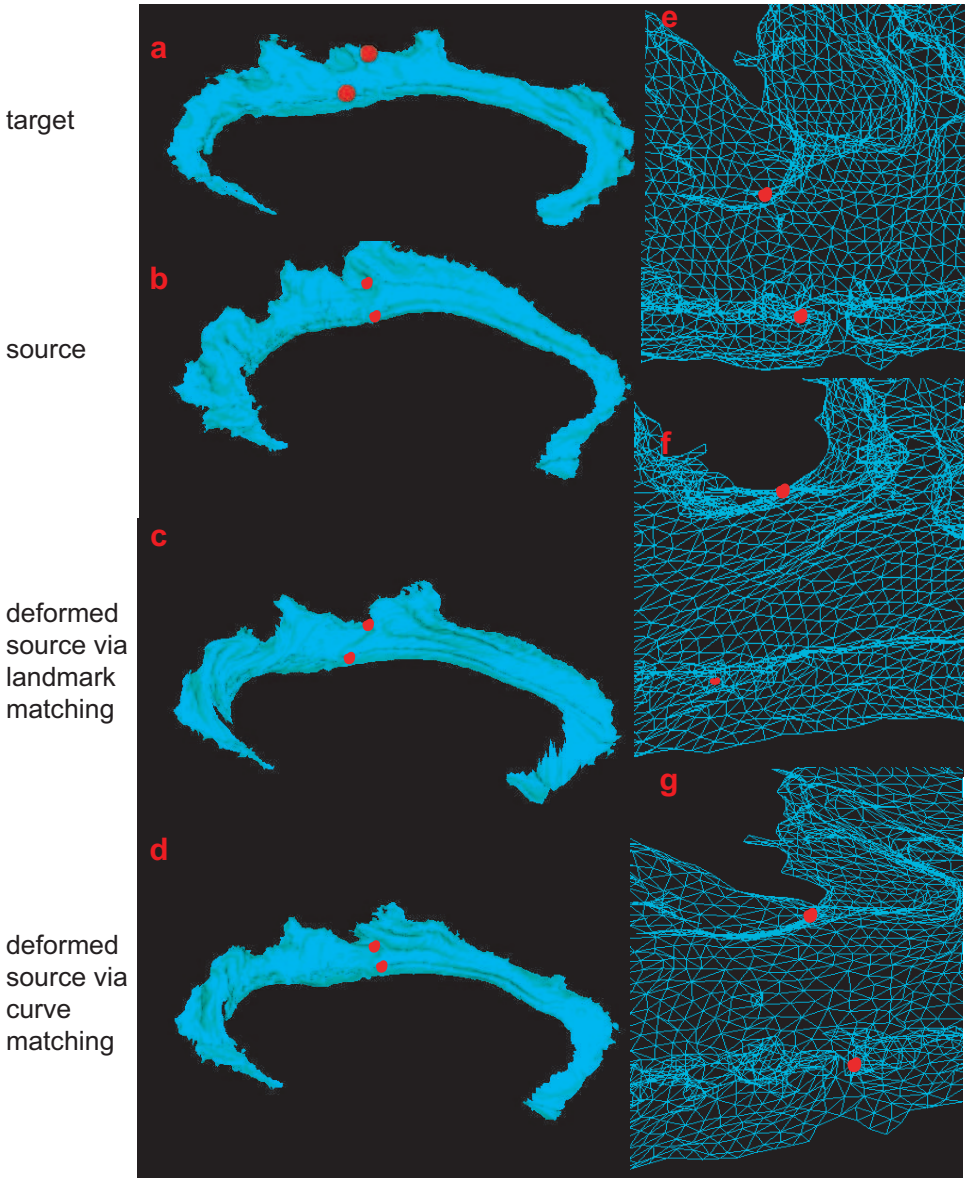

Figure 16: Comparison of deformation fields between the landmark and curve matchings. Panels (a-d) show the target, source, deformed source surface after the landmark matching, deformed source surface after the curve matching. Red dots represents paired landmarks on the target and source surfaces. Panels (e-g) show triangulated meshes respectively corresponding to the surfaces in panels (b-d).